Bedforms in a turbulent stream: formation of ripples by primary linear instability and of dunes by nonlinear pattern coarsening

ANTOINE FOURRIÈRE†, PHILIPPE CLAUDIN
AND BRUNO ANDREOTTI

Laboratoire de Physique et Mécanique des Milieux Hétérogènes, PMMH UMR 7636
CNRS-ESPCI-P6-P7, 10 rue Vauquelin, 75231 Paris Cedex 05, France

It is widely accepted that both ripples and dunes form in rivers by primary linear instability; the wavelength of the former scaling on the grain size and that of the latter being controlled by the water depth. We revisit here this problem in a theoretical framework that allows to give a clear picture of the instability in terms of dynamical mechanisms. A multi-scale description of the problem is proposed, in which the details of the different mechanisms controlling sediment transport are encoded into three quantities: the saturated flux, the saturation length and the threshold shear stress. Hydrodynamics is linearized with respect to the bedform aspect ratio. We show that the phase shift of the basal shear stress with respect to the topography, responsible for the formation of bedforms, appears in an inner boundary layer where shear stress and pressure gradients balance. This phase shift is sensitive to the presence of the free surface, and the related effects can be interpreted in terms of standing gravity waves excited by topography. The basal shear stress is dominated by this finite depth effect in two ranges of wavelength: when the wavelength is large compared to the flow depth, so that the inner layer extends throughout the flow, and in the resonant conditions, when the downstream material velocity balances the upstream wave propagation. Performing the linear stability analysis of a flat sand bed, the relation between the wavelength at which ripples form and the flux saturation length is quantitatively derived. It explains the discrepancy between measured initial wavelengths and predictions that do not take this lag between flow velocity and sediment transport into account. Experimental data are used to determine the saturation length as a function of grain size and shear velocity. Taking the free surface into account, we show that the excitation of standing waves has a stabilizing effect, independent of the details of the flow and sediment transport models. Consequently, the shape of the dispersion relation obtained from the linear stability analysis of a flat sand bed is such that dunes cannot result from a primary linear instability. We present the results of field experiments performed in the natural sandy Leyre river, which show the formation of ripples by a linear instability and the formation of dunes by a nonlinear pattern coarsening limited by the free surface. Finally, we show that mega-dunes form when the sand bed presents heterogeneities such as a wide distribution of grain sizes.

† Email address for correspondence: antoine.fourriere@espci.fr

1. Introduction

Since Richards (1980), and followed by others (Sumer & Bakioglu 1984; McLean 1990), ripples and dunes observed on the bed of sandy rivers have been interpreted as the two most unstable modes of the same linear instability. Although the classification of river bedform types is a difficult task (Ashley 1990), subaqueous ripples and dunes are standardly defined by their typical size: ripples are the small-scale bedforms whose wavelength λ scales on the grain size d and dunes are those whose wavelength is comparable to or larger than the flow depth H (Kennedy 1963; Engelund 1970; Fredsøe 1974; Richards 1980; Engelund & Fredsøe 1982; Allen 1985). A variant of this definition was used by Guy, Simons & Richardson (1966): dunes are the bed features larger than ripples that distort significantly the free surface and are out of phase with the standing waves they generate; ripples are the triangular shaped bedforms that have 'lengths of less than about 2 feet and heights of less than about 0.2 foot'. In some other articles (Hill, Srinivasan & Unny 1969; Yalin 1977), the classification of bedforms is rather based on the ratio of the grain diameter d to the viscous sublayer depth, i.e. on the particle Reynolds number $u_* d/\nu$ (u_* is the shear velocity and ν is the kinematic viscosity of the fluid). These criteria are questionable, especially when there is no clear separation of length scale between the spacing of ripple crests and the flow depth, and also in the case of bedforms superimposed on larger structures (Venditti, Church & Bennett 2005a). In this paper, willing to refer to the dynamical mechanisms involved in the formation of these bedforms, we shall call ripples those whose characteristics are independent of the flow depth; in contrast, dunes are directly related to the presence of a free surface. In particular, we shall not use the term 'sand wavelets', as suggested by Coleman *et al.* (Coleman & Melville 1994, 1996; Coleman & Eling 2000; Coleman, Fedele & Garcia 2003) to designate the initial stage of ripples when they emerge from a flat sand bed.

Experimental measurements on subaqueous ripples are numerous and exhibit large data dispersion. One of the reasons for such a dispersion is that ripples exhibit pattern coarsening, i.e. present a progressive increase of their typical length scale as time goes by (Mantz 1978; Gyr & Schmid 1989; Baas 1994; Coleman & Melville 1994, 1996; Baas 1999; Robert & Uhlman 2001; Coleman *et al.* 2003; Venditti, Church & Bennett 2005b; Langlois & Valance 2007; Rauen, Lin & Falconer 2008). Many authors have only measured fully developed wavelengths, whose relation with the initial wavelength λ is still an open issue. A reference database of final wavelengths in inclined flumes has been completed by Yalin (1985). Although not directly comparable to the predictions of a linear stability analysis, these data show distinct scaling laws for hydraulically smooth and rough granular beds. For a particle Reynolds number $u_* d/\nu$ smaller than few units, the viscous sublayer is larger than the grain size d and the fully developed ripple wavelength turns out to scale on ν/u_*, with a large – yet unexplained – prefactor ($\sim 10^3$). On the other hand, when the grain diameter d is larger than the viscous sublayer, the wavelength was found to slowly increase with u_*. Here we will focus on this hydraulically rough regime, in which the flow is turbulent at all scales down to the grain size. In several experimental articles (Baas 1994; Coleman & Melville 1994, 1996; Coleman & Eling 2000; Coleman *et al.* 2003; Langlois & Valance 2007), the initial wavelength λ has been carefully determined, showing scaling laws independent of the flow depth H. At large particle Reynolds number, λ is found to be almost independent of the shear velocity u_* and to increase with the grain diameter d (for instance Coleman *et al.* 2003 proposed $\lambda \propto d^{0.75}$). These measurements will serve as a benchmark for the theory developed in this paper.

Concerning dunes, most of the measurements have been performed in natural rivers, for which the Froude number $\mathscr{F}$ is low (see Best 2005 for a review). In the Mississipi river (Harbor 1998), in the Missouri river (Annambhotla, Sayre & Livesey 1972), in the Rhine (Carling *et al.* 2000; Wilbers & Ten Brinke 2003) and in the Rio Paraná (Parsons *et al.* 2005), the observed wavelengths range from $0.5H$ to $20H$ for Froude numbers around 0.2. The suggestion by Kennedy (1963) or Allen (1985) that dunes should present a well-selected wavelength scaling on $H/\mathscr{F}^2$ is thus far from reflecting the natural dispersion of field data. Flume experiments (see Guy *et al.* 1966; Robert & Uhlman 2001 and the data collected by Kennedy 1963) have been performed in a much larger range of Froude numbers (from 0.1 to 1) and also show well-developed bedform wavelengths between H and $30H$. The extensive data published by Guy *et al.* (1966) are particularly impressive, and the interested reader should refer to the original article rather than to the truncated data set plotted by Fredsøe (1974). We will discuss these data at the end of this article.

It has long been recognized that the mechanism responsible for the formation and growth of bedforms is related to the phase-lag between sediment transport and bed elevation (Kennedy 1963; Reynolds 1965; Kennedy 1969; Hayashi 1970; Smith 1970; Parker 1975; Engelund & Fredsøe 1982; McLean 1990). It has been shown in the context of aeolian dunes that this lag has two contributions, which can be considered as independent as the time scale involved in the bed evolution is much slower than the hydrodynamics relaxation (Andreotti, Claudin & Douady 2002; Kroy, Sauermann & Herrmann 2002; Valance 2005). First, there is a shift between the bed and the basal shear stress profiles. This shift purely results from hydrodynamics and its sign is not obvious *a priori*, i.e. the stress maximum can be either upstream or downstream of the bed crest depending on the topography or the proximity of the free surface. The second contribution comes from the sediment transport: the sediment flux needs some time/length to adapt to some imposed shearing (Bagnold 1941). This relaxation mechanism induces a downstream lag of the flux with respect to the shear. When the sum of these two contributions results in a maximum flux upstream of the bed crest, sediment deposition occurs on the bump, leading to an unstable situation and thus to the amplification of the disturbance.

We consider here the generic case of a flow over a fixed sinusoidal bottom of wavelength λ (see figure 1 for an illustration of the geometry and some notations). In order to obtain the basal shear stress and in particular its phase shift with respect to the topography, the equations of hydrodynamics must be solved in this geometry. The case of viscous flows has been investigated by Benjamin (1959), Bordner (1978), Caponi *et al.* (1982), Charru & Hinch (2000), Lagrée (2003) and Valance & Langlois (2005). The first attempts to model the high-Reynolds-number regime in the context of ripples and dunes in rivers have dealt with potential flows (Kennedy 1963; Reynolds 1965; Coleman & Fenton 2000), for which the velocity field does not present any lag with respect to the bottom. The shallow-water approximation (Gradowczyk 1970) implies that the bedforms spread their influence on the whole depth of the flow. However, patterns only have a significant influence within a vertical distance on the order of their wavelength. It is then crucial to compute explicitly the vertical flow structure, taking into account the turbulent fluctuations. In order to overcome the flaws of the perfect flow, constant eddy viscosity closures have been tried to improve Kennedy's original model (Engelund 1970; Smith 1970; Fredsøe 1974). Further progress has been made by Richards (1980), who used a more sophisticated modelling with an additional equation on the turbulent energy and a closure that involves a Prandtl mixing length in the expression of the eddy viscosity. Sumer & Bakioglu (1984) made
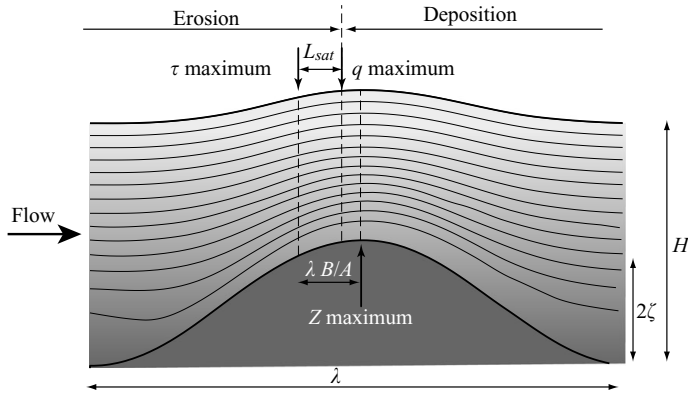
FIGURE 1. Schematic of the instability mechanism showing the streamlines around a bump. The fluid is flowing from left to right. A bump grows when the point at which the sand flux is maximum is located upwind the crest. The upwind shift of the maximum shear stress with respect to the crest has a hydrodynamical origin (factor B/A) and scales on the size of the bump λ. The spatial lag between the shear stress and the flux maxima is the saturation length L_{sat}.

use of the same turbulent modelling, but in the case of an infinite water depth. A mixing length approach was also used by Kobayashi & Madsen (1985) to improve Benjamin's laminar description.

In the meteorological context of atmospheric flows over low hills, a deep and fundamental understanding of the physics of turbulent flows over a relief has been developed from the 1970s (see the review by Belcher & Hunt 1998). Starting with the seminal work of Jackson & Hunt (1975), further refined by Sykes (1980) and Hunt, Leibovich & Richards (1988), the gross emerging picture is that the flow can be thought of as composed of three layers, associated with different physical mechanisms and different length scales. Jackson & Hunt (1975) have been able to compute analytically the basal shear stress for asymptotically large patterns, under an infinite flow depth assumption. Their ideas have been discussed in a rather vast literature. The predictions of these calculations, and in particular this layered structure of the flow, have been compared with experiments (see e.g. Britter, Hunt & Richards 1981; Gong & Ibbetson 1989; Finnigan *et al.* 1990) or field measurements on large-scale hills (see e.g. the review paper by Taylor, Mason & Bradley 1987), with a good degree of success, especially on the upstream side of the bumps. Moreover, they have been tested against the results of the numerical integration, in various configurations, of Navier–Stokes equations closed with different turbulent closures (Taylor 1977*a,b*; Richards & Taylor 1981; Ayotte, Xu & Taylor 1994). The relevance of this approach for the description of the flow and the stresses around aeolian sand dunes has also been investigated (see e.g. Weng *et al.* 1991) and is amongst the current directions of research in that community (Wiggs 2001).

As we shall see in this paper, the basal shear stress is generically found to be in phase advance with respect to the bottom profile (i.e. a destabilizing role) in the case of an unbounded flow. This means that, without any stabilizing mechanism, all wavelengths are found unstable. A key mechanism introduced by Fredsøe (1974) and kept in the following models is the stabilization of short wavelengths by a slope effect in the transport threshold. In these models, the preferred wavelength results from hydrodynamics and is proportional to the hydrodynamical roughness z_0 (or to ν/u_*

in the case of a viscous surface layer treated by Sumer & Bakioglu 1984). As shown by Charru (2006), the predicted ripple wavelengths are smaller than all experimental findings by several orders of magnitude.

In Kennedy (1963) and his followers (Reynolds 1965; Hayashi 1970; Smith 1970), a phenomenological spatial lag δ between the local sediment transport rate and the local velocity at the bottom of the outer layer is introduced. The phase shift between the sediment flux and the elevation profile is then simply $-2\pi\delta/\lambda$. This corresponds to a phase delay for $\lambda > 2\delta$, but to a phase advance for $\delta < \lambda < 2\delta$. As shown by Parker (1975), such a constant phase lag is not physically founded and the subsequent instability comes from a mathematical artefact. Rather, the adaptation of sediment transport to some imposed shearing can be described by a first-order relaxation equation of the form:

$$L_{sat}\partial_x q = q_{sat} - q. \tag{1.1}$$

where q_{sat} is the saturated (or equilibrium) flux, which is a function of the basal shear stress. This linear equation reflects the fact that the sand flux reaches its saturated value over a characteristic length L_{sat}. As for any other first-order system, the phase delay between the flux and the shear stress increases here from 0 for large wavelengths to $\pi/2$ for wavelengths much smaller than L_{sat} (i.e. a stabilizing role). The concept of flux saturation was correctly introduced in a linear stability analysis by Parker (1975), the flow being modelled by depth-averaged equations standardly used in hydraulics. However, these equations cannot describe the layered structure of the turbulent flow above bumps (Jackson & Hunt 1975), and in particular the so-called inner layer that is responsible for the phase shift between shear and topography. As a consequence, this author missed the explanation of the ripple instability.The idea that L_{sat} is the relevant length scale for the problem of dune formation was introduced in the aeolian context by Sauermann, Kroy & Herrmann (2001), Andreotti et al. (2002) and Kroy et al. (2002). Linear stability analysis developed in this context (Elbelrhiti, Claudin & Andreotti 2005; Claudin & Andreotti 2006; Andreotti & Claudin 2007) suggests that the initial wavelength actually scales on L_{sat}, and not on z_0. This line of thinking has been applied since then to subaqueous ripples (Valance 2005; Valance & Langlois 2005; Charru 2006). Importantly, although L_{sat} and z_0 are both ultimately related to the grain size d, they correspond to very different mechanisms associated with sediment transport and hydrodynamics, respectively.

Although Richards (1980) suggested that dunes could form by the same linear instability as ripples, no article has ever exhibited a proper and complete dispersion relation showing, in the same graph, the growth rate σ for a range of wavenumbers k that includes both ripples and dunes. In the figures provided by Richards (1980), σ is rescaled by k^2, which artificially enhances the small k (dunes) region. More recently, Colombini (2004) and Colombini & Stocchino (2005) revisited this problem, introducing that the thickness of the transport layer has a key parameter. This empirical refinement gives in practice an adjustable phase shift between relief and sand transport and allows to get a single well-defined peak in the dispersion relation, associated with dunes, at a wavelength on the order of the flow depth. However, this model does not predict the existence of a small-scale (ripple) instability anymore.

In this paper, we wish to discuss afresh this ripple and dune formation problem, and in particular to get such a complete dispersion relation where the peak associated with ripples is present. To reach this goal, we first describe the properties of a turbulent flow over a wavy bottom, generalizing Jackson & Hunt's analysis in the relevant range of wavelength $\lambda < 10^4 z_0$, for which their asymptotic matching is no more

valid, and in the presence of a free surface. We then show how to abstract the details of the transport mechanisms into a general framework with three key quantities, namely the saturated flux, the saturation length and the transport threshold. Mixing these ingredients, we show that the most unstable wavelength, corresponding to the ripple mode, is the product of a non-dimensional prefactor of hydrodynamical origin (destabilizing mechanism) by the transport saturation length (stabilizing mechanism). However, in contrast to Richards (1980), we show that dunes cannot form by a linear instability mechanism, and must rather result from the interaction and nonlinear pattern coarsening of ripples (Raudkivi & Witte 1990; Raudkivi 2006), limited by the free surface. This conclusion is supported by field experiments, performed in the Leyre river (France). Finally, we review and discuss the data available in the literature in the light of these theoretical and experimental results. Also, for the sake of concision, several tests of the robustness of our results, as well as some technical considerations of these calculations, are gathered in online supplementary appendices available at journals.cambridge.org/FLM.

2. Turbulent flow over a wavy bottom

2.1. *Turbulent flow over a uniform bottom*

2.1.1. *The logarithmic law*

We consider a turbulent flow over a relief. Following Reynolds' decomposition between average and fluctuating (denoted by a prime) quantities, the equations governing the mean velocity field u_i can be written as

$$\partial_i u_i = 0, \tag{2.1}$$

$$D_t u_i = \partial_t u_i + u_j \partial_j u_i = -\partial_j \tau_{ij} - \partial_i p, \tag{2.2}$$

where $\tau_{ij} = \overline{u_i' u_j'}$ is the Reynolds stress tensor (Reynolds 1874). For the sake of simplicity, we omit the density factor ρ in front of the pressure p and the stress tensor. The reference state is the homogeneous and steady flow over a flat bottom, submitted to an imposed constant shear stress $\tau_{xz} = -u_*^2$. The turbulent regime is characterized by the absence of any intrinsic length and time scales. At a sufficiently large distance z from the ground, the only length scale limiting the size of turbulent eddies – the so-called mixing length L – is precisely z; the only mixing time scale is given by the velocity gradient $|\partial_z u_x|$. As originally shown by Prandtl (1925), it results from this dimensional analysis that the only way to construct a diffusive flux is a turbulent closure of the form:

$$\tau_{xz} = -\kappa^2 L^2 |\partial_z u_x| \partial_z u_x, \tag{2.3}$$

where the mixing length is $L = z$ and $\kappa \simeq 0.4$ is the (phenomenological) von Kármán constant. After integration, one obtains that the velocity has a single non-zero component along the x axis, which increases logarithmically with z (Tritton 1988):

$$u_x = \frac{u_*}{\kappa} \ln\left(\frac{z}{z_0}\right), \tag{2.4}$$

where z_0 is the hydrodynamical roughness. This expression does not apply for $z \to 0$: there is a layer of thickness h_0 close to the bottom, called the surface layer, matching the logarithmic profile to a null velocity on the ground.

2.2. *Hydrodynamical roughness*

The hydrodynamical roughness z_0 should be distinguished from the geometrical (or physical) roughness of the ground, usually defined as the root mean square of the height profile variations. Note that z_0 is defined as the height at which the velocity would vanish, when extrapolating the logarithmic profile to small z; it is the constant of integration in (2.4). The physical mechanism controlling z_0 can be of different natures. If the ground is smooth enough, a viscous sublayer of typical size $O(\nu/u_*)$ must exist, whose matching with the logarithmic profile determines the value of z_0. On the contrary, if the geometrical roughness is larger than the viscous sublayer, turbulent mixing dominates at small z with a mixing length controlled by the ground topography. In the case of a flat static granular bed composed of grains of size d, reported values of the hydrodynamical roughness are reasonably consistent ($z_0 \simeq d/30$ in Bagnold 1941, $z_0 \simeq d/24$ in Schlichting & Gersten 2000 and $z_0 \simeq d/10$ in Kamphuis 1974; Andreotti 2004). The situation is of course different in the presence of sediment transport, which may (or not) induce a negative feedback on the flow. In this case, the hydrodynamical roughness z_0 may directly be controlled by the transport characteristics (e.g. mass flux and grain trajectories). We consider the asymptotic limit in which the typical relief length – say, the wavelength λ – is much larger than the surface layer thickness h_0. The relief is locally flat at the scale h_0, so there must be a region close to the ground where the velocity profile shows a logarithmic vertical profile. In the online Appendix, we discuss the case of moderate values of the ratio λ/h_0, for which the flow becomes sensitive to the details of the mechanisms controlling the roughness.

2.2.1. *A turbulent closure*

In the logarithmic boundary layer, the normal stresses can be written as

$$\tau_{xx} = \tau_{yy} = \tau_{zz} = \tfrac{1}{3}\tau_{ll} \qquad \text{with} \qquad \tau_{ll} = \kappa^2 \chi^2 L^2 |\partial_z u_x|^2, \tag{2.5}$$

where χ is a second phenomenological constant estimated in the range 2.5–3. Note that χ does not have any influence on the results as it describes the isotropic component of the Reynolds stress tensor, which can be absorbed into the pressure terms. Normal stress anisotropy can be easily taken into account, as explained in the online Appendix. Introducing the strain rate tensor $\dot{\gamma}_{ij} = \partial_i u_j + \partial_j u_i$ and its squared modulus $|\dot{\gamma}|^2 = (1/2)\dot{\gamma}_{ij}\dot{\gamma}_{ij}$, we can write both expressions (2.3) and (2.5) in a general tensorial form:

$$\boldsymbol{\tau}_{ij} = \kappa^2 L^2 |\dot{\gamma}| \left(\tfrac{1}{3}\chi^2 |\dot{\gamma}| \delta_{ij} - \dot{\boldsymbol{\gamma}}_{ij} \right). \tag{2.6}$$

In this paper, we focus on two-dimensional steady situations, i.e. on geometries invariant along the transverse y direction. As they are of permanent use for the rest of the paper, we express the components of the velocity and stress equations in the x and z directions. The Navier–Stokes equations read

$$\partial_x u_x + \partial_z u_z = 0, \tag{2.7}$$
$$u_x \partial_x u_x + u_z \partial_z u_x = -\partial_x p - \partial_z \tau_{xz} - \partial_x \tau_{xx}, \tag{2.8}$$
$$u_x \partial_x u_z + u_z \partial_z u_z = -\partial_z p - \partial_z \tau_{zz} - \partial_x \tau_{zx}. \tag{2.9}$$

The stress expressions are the following:

$$\tau_{xz} = -\kappa^2 L^2 |\dot{\gamma}|\dot{\boldsymbol{\gamma}}_{xz}, \tag{2.10}$$

$$\tau_{xx} = -\kappa^2 L^2 |\dot{\gamma}| \dot{\boldsymbol{\gamma}}_{xx} + \tfrac{1}{3}\kappa^2 \chi^2 L^2 |\dot{\gamma}|^2, \tag{2.11}$$

$$\tau_{zz} = -\kappa^2 L^2 |\dot{\gamma}| \dot{\boldsymbol{\gamma}}_{zz} + \tfrac{1}{3}\kappa^2 \chi^2 L^2 |\dot{\gamma}|^2. \tag{2.12}$$

In these expressions, the strain tensor components are given by

$$\dot{\boldsymbol{\gamma}}_{xz} = \dot{\boldsymbol{\gamma}}_{zx} = \partial_z u_x + \partial_x u_z, \quad \dot{\boldsymbol{\gamma}}_{xx} = 2\partial_x u_x \quad \text{and} \quad \dot{\boldsymbol{\gamma}}_{zz} = 2\partial_z u_z = -\dot{\boldsymbol{\gamma}}_{xx}, \tag{2.13}$$

and the strain modulus is given by

$$|\dot{\gamma}|^2 = 2(\partial_x u_x)^2 + 2(\partial_z u_z)^2 + (\partial_z u_x + \partial_x u_z)^2 = 4(\partial_x u_x)^2 + (\partial_z u_x + \partial_x u_z)^2. \tag{2.14}$$

2.3. *Linear perturbation analysis*

We now consider the turbulent flow over a wavy bottom constituting the floor of an unbounded boundary layer. In rivers, this corresponds to the limit of a flow depth H much larger than the bedform wavelength λ (ripples). The solution is computed as a first-order linear correction to the flow over a uniform bottom, using the first-order turbulent closure previously introduced.

2.3.1. *Linearized equations*

For small enough amplitudes, we can consider a bottom profile of the form

$$Z(x) = \zeta e^{ikx} \tag{2.15}$$

without loss of generality (real parts of expressions are understood). Note that $\lambda = 2\pi/k$ is the wavelength of the bottom and ζ is the amplitude of the corrugation; see figure 1. The case of an arbitrary relief can be deduced by a simple superposition of Fourier modes. We introduce the dimensionless variable $\eta = kz$, the dimensionless roughness $\eta_0 = kz_0$ and the function

$$\mathscr{U}(\eta) = \frac{1}{\kappa} \ln\left(\frac{\eta}{\eta_0}\right). \tag{2.16}$$

We perform the linear expansion of (2.7)–(2.14) with respect to the small parameter $k\zeta$. The mixing length is still defined as the geometrical distance to the bottom: $L = z - Z$. And we can write all the relevant quantities f under the generic form:

$$f(x, z) = \bar{f}(\xi) + k\zeta e^{ikx} \tilde{f}_1(\xi), \quad \text{with} \quad \xi = kz - kZ, \tag{2.17}$$

where $\bar{f}$ is the homogeneous field. Note that ξ is the curvilinear dimensionless coordinate. More explicitly, for the velocity and stress fields, we define the non-dimensional functions $\tilde{U}$, $\tilde{W}$, $\tilde{S}_t$, $\tilde{S}_n$, $\tilde{S}_{zz}$ and $\tilde{S}_{xx}$ by

$$u_x = u_* \left[\mathscr{U} + k\zeta e^{ikx} \tilde{U}\right], \tag{2.18}$$

$$u_z = u_* k\zeta e^{ikx} \tilde{W}, \tag{2.19}$$

$$\tau_{xz} = \tau_{zx} = -u_*^2 \left[1 + k\zeta e^{ikx} \tilde{S}_t\right], \tag{2.20}$$

$$p + \tau_{zz} = p_0 + u_*^2 \left[\frac{1}{3}\chi^2 + k\zeta e^{ikx} \tilde{S}_n\right], \tag{2.21}$$

$$\tau_{zz} = u_*^2 \left[\frac{1}{3}\chi^2 + k\zeta e^{ikx} \tilde{S}_{zz}\right], \tag{2.22}$$

$$\tau_{xx} = u_*^2 \left[\frac{1}{3}\chi^2 + k\zeta e^{ikx} \tilde{S}_{xx}\right]. \tag{2.23}$$

The study of the basal shear stress $\tilde{S}_t(0) \equiv A + iB$ constitutes the core of this section. The ratio B/A is the tangent of the phase shift between the shear stress and the topography.

An alternative way to perform the expansion is to use the Cartesian coordinate η and thus write the field f as

$$f(x, z) = \bar{f}(\eta) + k\zeta e^{ikx} f_1(\eta), \quad \text{with} \quad \eta = kz. \tag{2.24}$$

We call expressions (2.17) and (2.24) the 'shifted' and 'non-shifted' representations, respectively, of f – the tilde makes the distinction. The Taylor expansion shows that Cartesian and curvilinear systems of coordinates are simply related to each other, at the linear order in $k\zeta$, by

$$\tilde{f}_1 = f_1 + \bar{f}', \tag{2.25}$$

where the prime denotes the derivative. One can thus rigorously obtain the expression of $\tilde{f}_1$ from that of f_1, and reciprocally. Importantly, for the velocity U, the homogeneous field $\bar{f} = \mathscr{U}$ is not constant, so that $\tilde{U} = U + \mathscr{U}'$. By contrast, $\tilde{W} = W$, $\tilde{S}_t = S_t$ and $\tilde{S}_n = S_n$.

Although all possible representations are equivalent at the linear order in $k\zeta$, they differ at the nonlinear order, so that their domain of application is different. The range of amplitude ζ for which the solution of the linear problem is a good approximation of the full solution scales on z_0 for the non-shifted representation. By contrast, it scales on λ for the shifted representation. However, the linear equations are more compact in the non-shifted representation. As the passage from the shifted to the non-shifted representations is mathematically exact, we derive and solve the linear equations in the Cartesian system, and switch to the shifted representation afterwards: it leads to the same result to make a change of coordinates and linearize or to linearize and then make the change of coordinates. In particular, vertical profiles in the forthcoming figures will be mostly plotted as a function of the shifted variable ξ.

The linearized stress tensor reads:

$$\mathscr{U}' S_t = 2(U' + iW) - 2\kappa^2 \eta \mathscr{U}'^3, \tag{2.26}$$

$$\mathscr{U}' S_{xx} = -2iU + \tfrac{2}{3}\chi^2(U' + iW) - \tfrac{2}{3}\chi^2 \kappa \mathscr{U}'^2, \tag{2.27}$$

$$\mathscr{U}' S_{zz} = -2W' + \tfrac{2}{3}\chi^2(U' + iW) - \tfrac{2}{3}\chi^2 \kappa \mathscr{U}'^2, \tag{2.28}$$

and the Navier–Stokes equations lead to

$$W' = -iU, \tag{2.29}$$

$$S'_t = \mathscr{U}iU + \mathscr{U}'W + iS_n + iS_{xx} - iS_{zz}, \tag{2.30}$$

$$S'_n = -\mathscr{U}iW + iS_t. \tag{2.31}$$

Taking the difference of (2.27) and (2.28), one can compute

$$S_{xx} - S_{zz} = \frac{-4iU}{\mathscr{U}'} \tag{2.32}$$

to obtain four closed equations:

$$U' = -iW + \tfrac{1}{2}\mathscr{U}' S_t + \kappa \mathscr{U}'^2, \tag{2.33}$$

$$W' = -iU, \tag{2.34}$$

$$S'_t = \left(i\mathscr{U} + \frac{4}{\mathscr{U}'}\right) U + \mathscr{U}'W + iS_n, \tag{2.35}$$

$$S'_n = -i\mathscr{U}W + iS_t. \tag{2.36}$$

Introducing the vector $X = (U, W, S_t, S_n)$, we finally get at the first order in $k\zeta$ the following compact form of the equation to integrate:

$$\frac{d}{d\eta}X = \mathscr{P}X + S, \quad \text{with} \quad \mathscr{P} = \begin{pmatrix} 0 & -i & \frac{1}{2}\mathscr{U}' & 0 \\ -i & 0 & 0 & 0 \\ (i\mathscr{U} + \frac{4}{\mathscr{U}'}) & \mathscr{U}' & 0 & i \\ 0 & -\mathscr{U}i & i & 0 \end{pmatrix} \quad \text{and} \quad S = \begin{pmatrix} \kappa\mathscr{U}'^2 \\ 0 \\ 0 \\ 0 \end{pmatrix}. \tag{2.37}$$

The general solution of this equation is the linear superposition of all solutions of the homogeneous system (i.e. with $S = 0$), and a particular solution X_s.

2.3.2. *Boundary conditions*

Four boundary conditions must be specified to solve (2.37). The upper boundary corresponds to the limit $\eta \to \infty$, in which the vertical fluxes of mass and momentum vanish asymptotically. This means that the first-order corrections to the shear stress and to the vertical velocity must tend to zero: $W(\infty) = 0$ and $S_t(\infty) = 0$. In practice, a boundary at finite height H (at $\eta_H = kH$) is introduced, at which we impose a null vertical velocity $W(\eta_H) = 0$ and a constant tangential stress $-u_*^2$ so that $S_t(\eta_H) = 0$. This corresponds to a physical situation in which the fluid is entrained by a moving upper plate, for instance a stress-controlled Couette annular cell. Then, we consider the limit $H \to +\infty$, i.e. when the results become independent of H.

The lower boundary condition must be specified on the floor ($\eta \to kZ$). We consider here the limit in which the surface layer thickness h_0 is much smaller than the wavelength λ. This allows to perform an asymptotic matching between the solution and the surface layer, whatever the dynamical mechanisms responsible for the hydrodynamical roughness z_0 are. Indeed, focusing on the surface layer, we know that in the limit $z \gg h_0$, the asymptotic behaviour of the local tangential velocity u should be a logarithmic profile controlled by the local shear stress τ and the roughness z_0. The solution of (2.37) should thus match this asymptotic behaviour as $\eta \to kZ$. Thus, z_0 is the only parameter inherited from the surface layer in the limit $h_0 \ll \lambda$.

In the limit $z - Z \ll \lambda$, the homogeneous solution of (2.37) can be expanded in power series of the form $\eta^\alpha \ln^\beta(\eta/\eta_0)$ and presents four degrees of freedom. The full solution reads

$$X \underset{\eta \to 0}{\sim} a_1 \begin{pmatrix} \mathscr{U}^2/4 \\ 1 \\ \mathscr{U} \\ -\eta^2\mathscr{U}^3/4 \end{pmatrix} + a_2 \begin{pmatrix} \mathscr{U}/2 \\ -i\eta\,\mathscr{U}/2 \\ 1 \\ i\eta \end{pmatrix} + a_3 \begin{pmatrix} 1 \\ -i\eta \\ i\eta\,\mathscr{U}(\eta) \\ -\eta^2\,\mathscr{U}(\eta) \end{pmatrix} + a_4 \begin{pmatrix} i\eta/(2\kappa) \\ \eta^2/(4\kappa) \\ i\eta \\ 1 \end{pmatrix} + X_s, \tag{2.38}$$

where $X_s = (-(1/\kappa\eta), (i/\kappa)\ln(\eta/\eta_0), 0, 0)$ is the asymptotic behaviour of the particular solution. The following terms in this expansion are $O(\eta\ln^2(\eta/\eta_0))$.

The values of the four coefficients $a_1, \dots, a_4$ are selected by matching with the surface layer. Note that a_1 corresponds to a non-vanishing normal velocity through the surface layer and should thus be null. Note also that a_2 precisely corresponds to the logarithmic profile with a roughness z_0 and a basal shear stress modulation a_2. This gives $a_2 = S_t(0)$. Similarly, a_3 corresponds to a modulation of the local

roughness – more precisely of its logarithm. We do not consider such a modulation so that $a_3 = 0$. Likewise, a_4 corresponds to a sub-dominant behaviour associated with the basal pressure modulation ($a_4 = S_n(0)$). In summary, the functions U, W, S_t and S_n should follow the following asymptotic behaviour:

$$U(\eta) = \frac{S_t(0)}{2\kappa} \ln \frac{\eta}{\eta_0} + \frac{iS_n(0)}{2\kappa}\eta - \frac{1}{\kappa\eta}, \tag{2.39}$$

$$W(\eta) = -\frac{iS_t(0)}{2\kappa}\eta \left(\ln \frac{\eta}{\eta_0} - 1 \right) + \frac{S_n(0)}{4\kappa}\eta^2 + \frac{i}{\kappa} \ln \frac{\eta}{\eta_0}, \tag{2.40}$$

$$S_t(\eta) = S_t(0) + iS_n(0)\eta, \tag{2.41}$$

$$S_n(\eta) = S_n(0). \tag{2.42}$$

The region of thickness ℓ in which this asymptotic behaviour constitutes a good approximation of the flow field is called the inner layer. Equation (2.42) means that the total pressure $\wp = p + \tau_{ll}/3$ is constant across this boundary layer:

$$\partial_z \wp = 0 \tag{2.43}$$

and (2.41) that the shear stress decreases linearly with height according to

$$\partial_x \wp + \partial_z \tau_{xz} = 0. \tag{2.44}$$

The tangential pressure gradient is balanced by the normal shear stress, which means that inertial terms are negligible or equivalently that the fluid is in local equilibrium. In terms of energy, the space variation of the internal energy (pressure) is dissipated in 'turbulent friction'. These two equations correspond to the standard lubrication approximation for quasi-parallel flows.

2.4. *Solving equations*

In practice, we solve the equations using a fourth-order Runge–Kutta scheme with a logarithmic step. The integration is started at an initial value of η inside the inner layer which verifies $\eta \ln^2(\eta/\eta_0) \ll 1$. We write the solution as a linear superposition of the form $\mathbf{X} = \mathbf{X}_s + S_t(0)\mathbf{X}_t + S_n(0)\mathbf{X}_n$, where the different terms verify

$$\frac{d}{d\eta}\mathbf{X}_s = \mathscr{P}\mathbf{X}_s + \mathbf{S} \quad \text{starting from} \quad \mathbf{X}_s(\eta) = \left(-\frac{1}{\kappa\eta}, \frac{i}{\kappa} \ln \frac{\eta}{\eta_0}, 0, 0 \right), \tag{2.45}$$

$$\frac{d}{d\eta}\mathbf{X}_t = \mathscr{P}\mathbf{X}_t \quad \text{starting from} \quad \mathbf{X}_t(\eta) = \left(\frac{1}{2\kappa} \ln \frac{\eta}{\eta_0}, -\frac{i\eta}{2\kappa}\left[\ln \frac{\eta}{\eta_0} - 1 \right], 1, 0 \right), \tag{2.46}$$

$$\frac{d}{d\eta}\mathbf{X}_n = \mathscr{P}\mathbf{X}_n \quad \text{starting from} \quad \mathbf{X}_n(\eta) = \left(\frac{i\eta}{2\kappa}, \frac{\eta^2}{4\kappa}, \eta, 1 \right). \tag{2.47}$$

The boundary conditions on the bottom are then automatically satisfied, and the top ones give algebraic equations on the real and imaginary parts of $S_t(0)$ and $S_n(0)$, which can be solved easily. We have checked that the result is independent of the initial value of η, as long as it remains in the announced range.

2.4.1. *Results*

The velocity and stress profiles resulting from the integration of (2.37) are displayed in figure 2. In figure 2(*c*), one can clearly see the region close to the bottom where the shear stress is constant, whereas the horizontal velocity component (figure 2*a*) exhibits a logarithmic behaviour. This plateau almost coincides with the inner layer, which is the zone where the solution is well approximated by the asymptotic behaviour derived
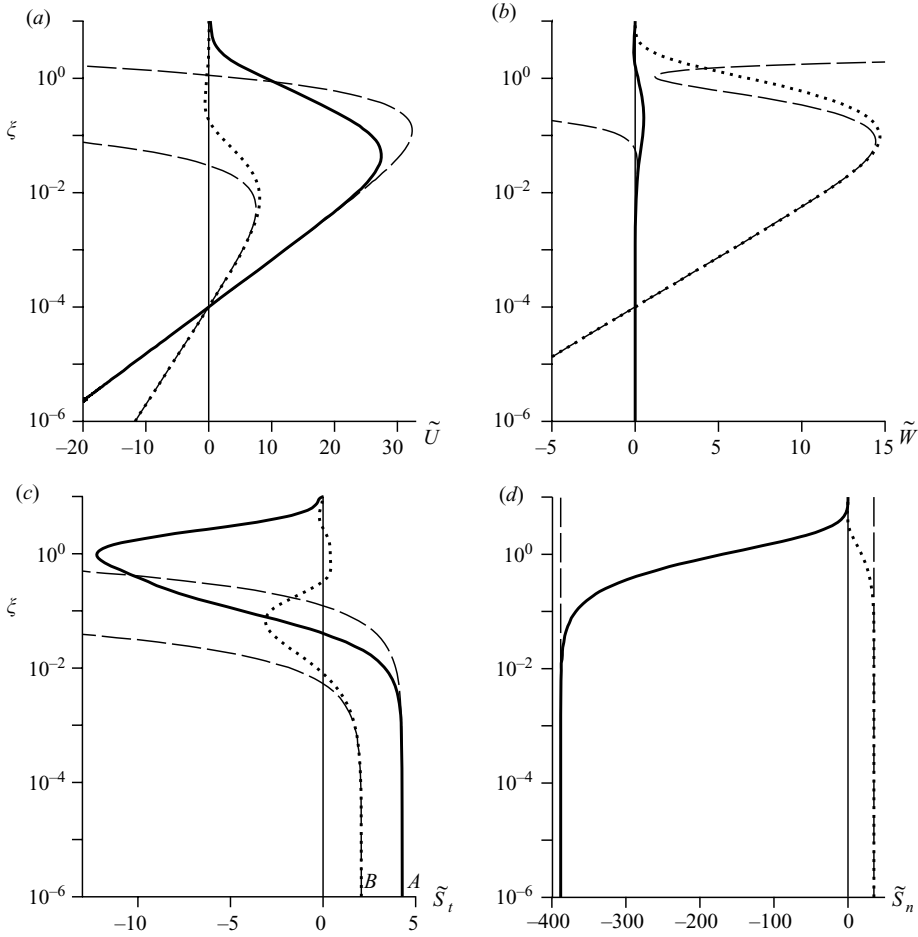
FIGURE 2. Vertical profiles of the first-order corrections to velocities and stresses for $\eta_0 = 10^{-4}$. $\xi = \eta - kZ$ is the distance to the bottom, rescaled by the wavenumber. In $(a$–$d)$, the solid lines represent the real parts of the functions, whereas the dotted lines represent the imaginary ones. Dashed lines show the asymptotic behaviours (2.39)–(2.42) used as boundary conditions. They match the solutions in the inner layer, which extends up to $\eta \simeq k\ell \simeq 10^{-2}$ here. Close to the boundary, a plateau of constant shear stress can be observed ($\tilde{S}_t(0) = A + iB$), which corresponds to the logarithmic zone. It is embedded into a slightly larger zone of constant pressure in which the shear stress varies linearly.

above. The inner layer is embedded in a wider region characterized by a constant pressure (figure 2*d*). The thickness ℓ of the inner layer is the scale at which inertial terms are of the same order as stress ones in the Reynolds averaged Navier–Stokes equations. The original estimation of ℓ given by Jackson & Hunt (1975) was further discussed in several later papers (see e.g. Taylor *et al.* 1987; Claussen 1988; Beljaars & Taylor 1989; Finnigan *et al.* 1990). Our data are in good agreement with the scaling proposed by Taylor *et al.* (1987):

$$\frac{\ell}{\lambda} \frac{1}{\kappa^2} \ln^2 \frac{\ell}{z_0} = O(1). \tag{2.48}$$

Consistently, this scaling relationship is precisely that obtained when considering the first neglected terms in the asymptotic expansion (2.38). Away from the bottom, all
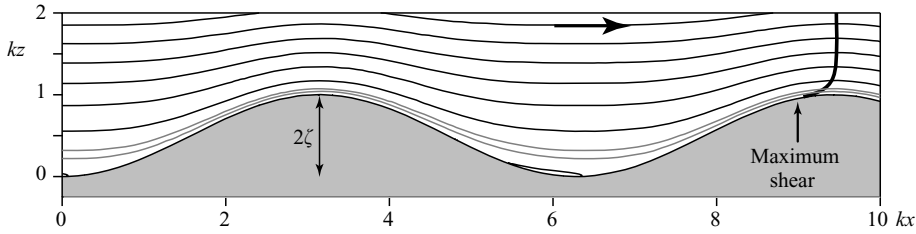
FIGURE 3. Flow streamlines above a wavy bottom of rescaled amplitude $k\zeta = 0.5$ (aspect ratio $\sim 1/6$), computed from the linearized equations ($\eta_0 = 10^{-4}$). The flow direction is from left to right. Note the left–right asymmetry of the streamlines around the bump in the inner layer (grey lines). Note also the onset of emergence of a recirculation bubble in the troughs. The thick line in the top right corner shows the positions that maximizes the velocity along a streamline.

profiles tend to zero, so that one recovers the undisturbed flow field (2.4) at large η. The shape of these profiles is very consistent with the work of Ayotte *et al.* (1994), who have compared the influence of the closure scheme on the linear flow over a relief, which means that the precise choice of the turbulent closure does not significantly affect the results.

In order to visualize the effect of the bottom topography on the flow, the flow streamlines are displayed in figure 3 (see the online Appendix for details about streamlines computation). It can be observed that the velocity gradient is larger on the crest than in the troughs as the streamlines are closer to each other. The flow is disturbed over a vertical distance comparable to the wavelength. A subtler piece of information concerns the position along each streamline at which the velocity is maximum. These points are displayed in the right corner of figure 3. Away from the bottom, they are aligned above the crest of the bump. Very close to it, however, they are shifted upstream. In other words, the fluid velocity is in phase with the topography in the upper part of the flow, but is phase advanced in the inner boundary layer where the shear stress tends to its basal value. In this inner layer, the profile is well approximated by its asymptotic expression (2.39). In the outer region ($\eta \gg k\ell$), U decreases exponentially with the distance to the bottom (figure 2). Seeking for asymptotic solutions decreasing as $e^{-\sigma\eta}$, one has to solve the eigenvalue problem $\mathscr{P}X = -\sigma X$ for asymptotically large values of η. At the two leading orders, the decrease rate σ is given by

$$2i\left(\sigma^4 + 1\right)\kappa^2\eta + \left(\sigma^2 - 1\right)\ln\frac{\eta}{\eta_0} = 0. \tag{2.49}$$

The asymptotic behaviour is an oscillatory relaxation corresponding to $\sigma = (1 \pm i)/\sqrt{2}$. However, the observed decrease corresponds to the intermediate asymptotic regime $\eta < \ln(\eta/\eta_0)$ for which the solution is $\sigma = 1$. This behaviour is reminiscent from that of an inviscid potential flow. In other words, the effect of the turbulent shear stress on the flow disturbance can be neglected, in this external layer.

The intermediate region between the inner and the outer layers is responsible for the asymmetry of the flow as well as the upstream shift of the maximum velocity discussed above. Let us emphasize again that this is the physical key point for the formation of ripples. One can understand the reason of the phase shift with the following physical argument. The external layer can be described as a perfect irrotational flow. Since the elevation profile is symmetric, the streamlines are symmetric too, as the flow is solely
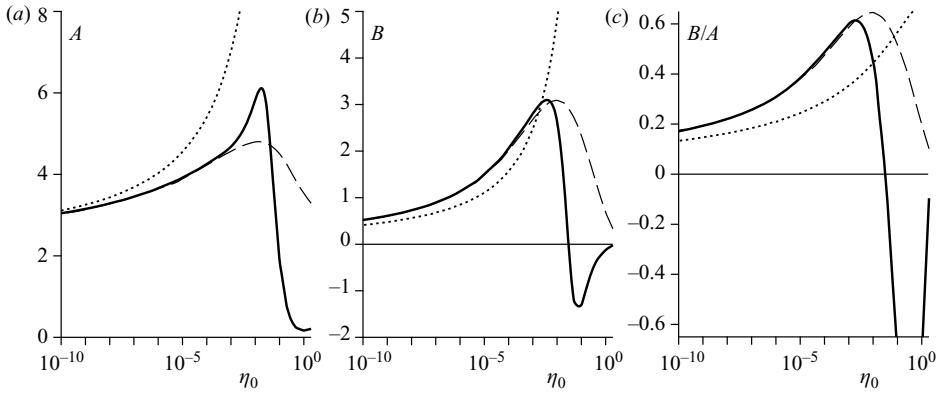
FIGURE 4. Coefficients A, B and ratio B/A as a function of $\eta_0 = kz_0$. These plots show the dependence of the basal shear and normal stresses with the number of decades separating the wavelength λ from the soil roughness z_0. The solid line corresponds to the results of the model, using the asymptotic matching with the surface layer ($L = z - Z$). The dotted lines correspond to a phenomenological mixing length $L = z_0 + z - Z$. The dashed lines correspond to the approximation used by Jackson & Hunt (1975). All curves agree well at very small η_0.

controlled by the balance between inertia and the pressure gradient induced by the presence of the bump. As a consequence, the velocity is maximum at the vertical of the crest. Now, inside the inner layer, this flow is slowed down by turbulent diffusion of momentum. Focusing on the region of matching between these outer and inner regions, the velocity needs some time to re-adapt to a change of shear stress, due to inertia. Thus, the shear stress is always phase advanced with respect to the velocity. One concludes that the basal shear stress is phase advanced with respect to the bump.

The basal shear stress component in phase (A) and in quadrature (B) with the topography is displayed as a function of η_0 in figure 4. The ratio B/A is positive as the shear stress is phase advanced. Their overall dependence with η_0 is weak, meaning that the turbulent flow around an obstacle is mostly scale invariant. More precisely, following Jackson & Hunt (1975), Kroy *et al.* (2002) have shown that, for asymptotically small η_0, one expects logarithmic dependencies:

$$A = \frac{\ln^2\left(\Phi^2/\ln\Phi\right)}{2\ln^3\phi}\left(1 + \ln\phi + 2\ln\frac{\pi}{2} + 4\gamma_E\right) \quad \text{and} \quad B = \pi\frac{\ln^2\left(\Phi^2/\ln\Phi\right)}{2\ln^3\phi}, \quad (2.50)$$

where $\gamma_E \simeq 0.577$ is Euler's constant, ϕ is defined by the equation $\phi\ln\phi = 2\kappa^2\Phi$ and with $\Phi = \pi/(2\eta_0)$. Note that A tends to 2 and B to 0 as $\eta_0 \to 0$, as expected when the inner layer thickness ℓ vanishes. In this limit, the basal shear stress is directly proportional to the square of the velocity inherited from the outer layer, which is solution of the potential flow problem. These expressions agree well with our numerical results for very small η_0. However, for realistic values of η_0, e.g. $10^{-4} < \eta_0 < 10^{-2}$, this approximation cannot be accurately used as it leads to errors of order one – note that Jackson & Hunt's expressions tend to diverge at larger η_0.

Figure 4 also shows the results obtained for a particular model of surface layer, which describes an hydrodynamically rough bottom. Then, the 'small scale' roughness elements are larger than the viscous sublayer. They are submitted to a turbulent drag from the fluid, and reciprocally, their presence slows down the flow. The exchanges of momentum in the surface layer are thus dominated by the turbulent fluctuations. Following Richards (1980) and others, a convenient phenomenological model is to

define the mixing length involved in the turbulent closure (2.6) as $L = z_0 + z - Z$. In this way, L is still essentially the geometrical distance to the bottom, except that it cannot be smaller than the roughness length. This choice reflects, in an intuitive manner, the physical picture one can infer from experiments or simulations where square-shaped roughness elements are glued on a flat wall (see e.g. Perry, Schofield & Joubert 1969). One can see in figure 4 that, for $\eta_0 < 10^{-3}$, the values of A and B match those obtained using the asymptotic matching with the surface layer. However, one can note significant differences for $\eta_0 > 10^{-2}$. As the mixing length in the surface layer is larger in this case ($L \sim z_0$) than that in the asymptotic case ($L \sim z - Z$), the turbulent 'diffusion' is more efficient. This results into a larger phase advance for the shear stress (figure 4c).

In the online Appendix, we have tested the robustness of the results with respect to the details of the model. The phase lag between the shear stress and the elevation profile is mostly insensitive to:

(i) the introduction of a lag between the turbulent energy and the mean strain tensor (second-order turbulent closure),

(ii) the Reynolds stress tensor anisotropy,

(iii) the dynamical mechanisms controlling the surface layer at moderate values of the ratio λ/h_0, and

(iv) a moving bottom, either growing or propagating.

In conclusion, for the study of ripples and dunes, these effects can be safely ignored. In particular, the sediment bed can be considered as fixed to compute the flow field.

2.5. *Effect of a free surface*

In this section, we investigate the effect of the additional presence of a free surface at a finite distance H to the bottom. This situation is relevant to the flow above river dunes.

2.5.1. *River equilibrium*

In the case of a river inclined at an angle θ on the horizontal, the shear stress must balance gravity. It thus varies linearly as $\tau_{xz} = g(z - H)\sin\theta$ and vanishes at the free surface. By definition of the shear velocity u_*, we also write $\tau_{xz} \equiv u_*^2(z/H - 1)$. In the context of a mixing length approach to describe turbulence, this length should vanish at the free surface. For the sake of simplicity, we take $L = (z + z_0)\sqrt{1 - z/H}$. This choice results in a base flow that is logarithmic, as in the unbounded situation:

$$u_x = \frac{u_*}{\kappa}\ln\left(1 + \frac{z}{z_0}\right), \tag{2.51}$$

which is consistent with field and experimental observations. The stress balance equation along the z axis allows to get the pressure, which reads

$$p + \tau_{zz} = p_0 + g(H - z)\cos\theta = p_0 + \frac{u_*^2}{\tan\theta}\left(1 - \frac{z}{H}\right). \tag{2.52}$$

We define the Froude number as the ratio of the surface velocity $u_{surface}$ to the velocity of gravity surface waves in the shallow-water approximation:

$$\mathscr{F} \equiv \frac{u_{surface}}{\sqrt{gH}} \equiv \frac{1}{\sqrt{gH}}\frac{u_*}{\kappa}\ln\left(1 + \frac{H}{z_0}\right) = \frac{1}{\kappa}\ln\left(1 + \frac{H}{z_0}\right)\sqrt{\sin\theta}. \tag{2.53}$$

In the literature, the Froude number is sometimes defined as the ratio of the mean velocity to the velocity of gravity waves. We will justify this choice in the next

paragraph. The Froude number of natural sandy rivers lies in general between 0.1 and 0.3 as they flow on very small slopes. Larger Froude numbers are reached in flume experiments.

2.5.2. *Disturbances*

As above, we consider a wavy bottom $Z = \zeta e^{ikx}$ and note again $\eta = kz$ and $\eta_H = kH$. We write the first-order corrections to the base flow as

$$u_x = u_* \left[\mathscr{U} + k\zeta e^{ikx} U \right],$$ (2.54)

$$u_z = u_* k\zeta e^{ikx} W,$$ (2.55)

$$\tau_{xz} = \tau_{zx} = -u_*^2 \left[1 - \frac{\eta}{\eta_H} + k\zeta e^{ikx} S_t \right],$$ (2.56)

$$p + \tau_{zz} = p_0 + u_*^2 \left[\frac{1}{\tan\theta} \left(1 - \frac{\eta}{\eta_H} \right) + k\zeta e^{ikx} S_n \right],$$ (2.57)

where, in accordance with (2.51), the function $\mathscr{U}$ is defined by the relation

$$\mathscr{U}(\eta) = \frac{1}{\kappa} \ln\left(1 + \frac{\eta}{\eta_0} \right).$$ (2.58)

The free surface is also disturbed by the presence of the non-uniform bottom, and we denote by $H + \Delta(x)$ the flow depth at the position x. The modified expression for the mixing length then reads

$$L = (z_0 + z - Z)\sqrt{\frac{H + \Delta - z}{H + \Delta - Z}}.$$ (2.59)

Linearizing the free surface profile as $\Delta(x) = \delta\zeta e^{ikx}$, L expends to the first order into

$$kL = (\eta + \eta_0)\sqrt{1 - \frac{\eta}{\eta_H}} \left\{ 1 - k\zeta e^{ikx} \left[\frac{1}{\eta + \eta_0} - \frac{1}{2\eta_H} - \delta \frac{\eta}{2\eta_H^2 \left(1 - \frac{\eta}{\eta_H} \right)} \right] \right\}.$$ (2.60)

The shear stress closure as well as the Reynolds averaged Navier–Stokes equations can be linearized in the same way as before, and we finally get at the first order in $k\zeta$ a system of differential equations that can be written under the following form:

$$\frac{\mathrm{d}}{\mathrm{d}\eta} X = \mathscr{P} X + S + \delta S_\delta,$$ (2.61)

with

$$\mathscr{P} = \begin{pmatrix} 0 & -i \dfrac{\mathscr{U}'}{2\left(1 - \dfrac{\eta}{\eta_H} \right)} & 0 \\ -i & 0 & 0 & 0 \\ \dfrac{4}{\mathscr{U}'}\left(1 - \dfrac{\eta}{\eta_H} \right) + i\mathscr{U} & \mathscr{U}' & 0 & i \\ 0 & -\mathscr{U}i & i & 0 \end{pmatrix},$$ (2.62)
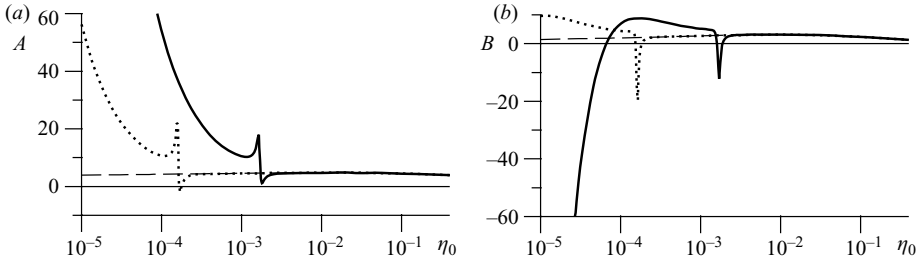
FIGURE 5. A and B as functions of η_0 for $\mathscr{F} = 0.8$ and $H/z_0 = 10^3$ (solid line) or $H/z_0 = 10^4$ (dotted line). The dashed line corresponds to the unbounded case (the same as in figure 4). The curves collapse at large η_0 but differ at small η_0, showing a resonance peak and a divergence at $\eta_0 \to 0$.

$$
S = \begin{pmatrix} \kappa \mathscr{U}'^2 - \dfrac{\mathscr{U}'}{2\eta_H} \\ 0 \\ 0 \\ 0 \end{pmatrix}, \quad \text{and} \quad \vec{S}_\delta = \begin{pmatrix} -\dfrac{\eta \mathscr{U}'}{2\eta_H^2 \left(1 - \dfrac{\eta}{\eta_H}\right)} \\ 0 \\ 0 \\ 0 \end{pmatrix}. \tag{2.63}
$$

2.5.3. *Resolution of the linearized equations*

Again, making use of the linearity of the equations, we seek the solution under the form $X = X_0 + a_t X_t + a_n X_n + \delta X_\delta$, where these vectors are solution of the following equations:

$$
\frac{\mathrm{d}}{\mathrm{d}\eta} X_s = \mathscr{P} X_s + S \qquad \text{with} \quad X_s(0) = \left(-\frac{1}{\kappa \eta_0}, 0, 0, 0\right), \tag{2.64}
$$

$$
\frac{\mathrm{d}}{\mathrm{d}\eta} X_t = \mathscr{P} X_t \qquad \text{with} \quad X_t(0) = (0, 0, 1, 0), \tag{2.65}
$$

$$
\frac{\mathrm{d}}{\mathrm{d}\eta} X_n = \mathscr{P} X_n \qquad \text{with} \quad X_n(0) = (0, 0, 0, 1), \tag{2.66}
$$

$$
\frac{\mathrm{d}}{\mathrm{d}\eta} X_\delta = \mathscr{P} X_\delta + S_\delta \qquad \text{with} \quad X_\delta(0) = (0, 0, 0, 0). \tag{2.67}
$$

The bottom boundary conditions $U(0) = -1/(\kappa \eta_0)$ and $W(0) = 0$ are then automatically satisfied. At the free surface, we impose the material nature of the surface, $W(\eta_H) = i\mathscr{U}(\eta_H)\delta$, and vanishing stresses: $S_t(\eta_H) = \delta/\eta_H$ and $S_n(\eta_H) = \delta/(\eta_H \tan\theta)$. These last three conditions select the coefficients a_t and a_n as well as the value of δ. Finally, note that the analytical approximation of the solution close to the bottom in the limit $\eta_0 \to 0$ is the same as in the unbounded case – it does not depend on the position of the upper boundary – and expressions (2.39)–(2.42) are thus still correct in the limit $H \gg z_0$.

2.5.4. *Results*

In order to evidence the role of the free surface, we have plotted the stress coefficients A and B as functions of η_0 in figure 5, for different values of H/z_0. For a large enough wavenumber k (a small enough wavelength λ), one recovers the unbounded case. This means that for a bottom wavelength much smaller than the flow depth H (i.e. for subaqueous ripples), the free surface has a marginal effect and the results of §2.3
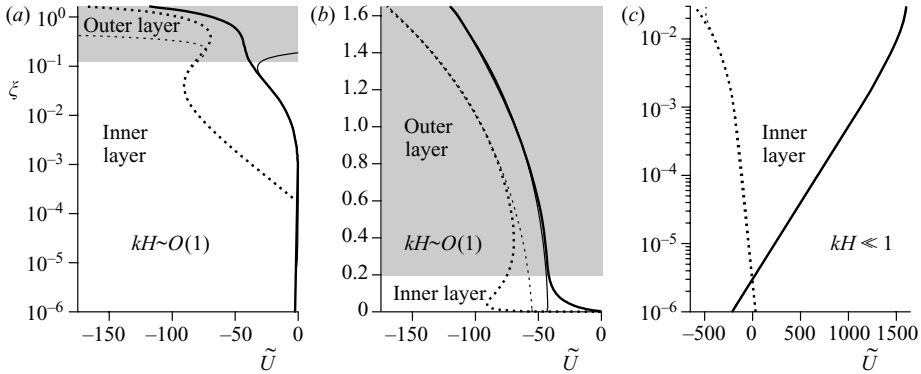
FIGURE 6. Relative importance of the inner (white) and outer (grey) layers for $kH = 1.65$ (a, b), and $kH = 0.03$ (c), with $H/z_0 = 10^4$. The velocity profiles (bold lines) are compared with their asymptotic behaviour in the inner and outer layers (thin lines). The solid lines represent the real part of the functions, and the dotted lines represent the imaginary ones. (a) and (b) show the very same profile, but with a logarithmic scale in (a) to emphasize the inner region. The thin lines in (a) and (c) represent the asymptotic behaviour in the inner layer. Those in (b) correspond to a sum of an increasing and a decreasing exponential of the form $\exp(\pm\eta)$, as for an inviscid potential flow.

apply. For smaller η_0, however, the curves exhibit a peak, whose position depends on the value of H/z_0, followed by a diverging behaviour when $\eta_0 \to 0$. As discussed below, this peak can be ascribed to a resonance of standing waves at the free surface, excited by the bottom topography, meaning that the proper scale is now H and not z_0.

The analysis of velocity profiles for different values of kH gives the following physical picture (figure 6). For $kH > 1$, as for the unbounded case, the flow can be thought of as being divided into two regions: an inner layer close to the bottom, where it can be described by the equilibrium approximation, and an outer layer behaving like an inviscid potential flow, where the profiles can be decomposed into the sum of decreasing and increasing exponentials $e^{\pm\eta}$. For smaller values of kH, this outer region progressively vanishes and the whole flow is controlled by the inner layer.

We display the phase and amplitude of the free surface as a function of kH in figure 7(b,c). The peak in amplitude accompanied by the phase shift of π are the signature of a surface wave resonance. The source of disturbances is the bedform relief. For kH larger than its resonant value, the bottom and the free surfaces are in phase; conversely, for kH below the resonance, they are in antiphase. In between, at the resonance, the phase shift is $\varphi = \pi/2$ (figure 7a) so that the streamlines are squeezed downstream of the crest. This resonance is model independent as it comes from a very robust physical mechanism. As the fluid flows over the periodic bottom, gravity surface waves are excited at the wavelength λ. The latter propagate at the velocity:

$$c \simeq u_{surface} \pm \sqrt{\frac{g}{k}\tanh(kH)} = \mathscr{F}\sqrt{gH} \pm \sqrt{\frac{g}{k}\tanh(kH)} \qquad (2.68)$$

with respect to the bottom. As in the sound barrier phenomenon, the wave energy induced by the bottom disturbances accumulates when this velocity vanishes, i.e. for

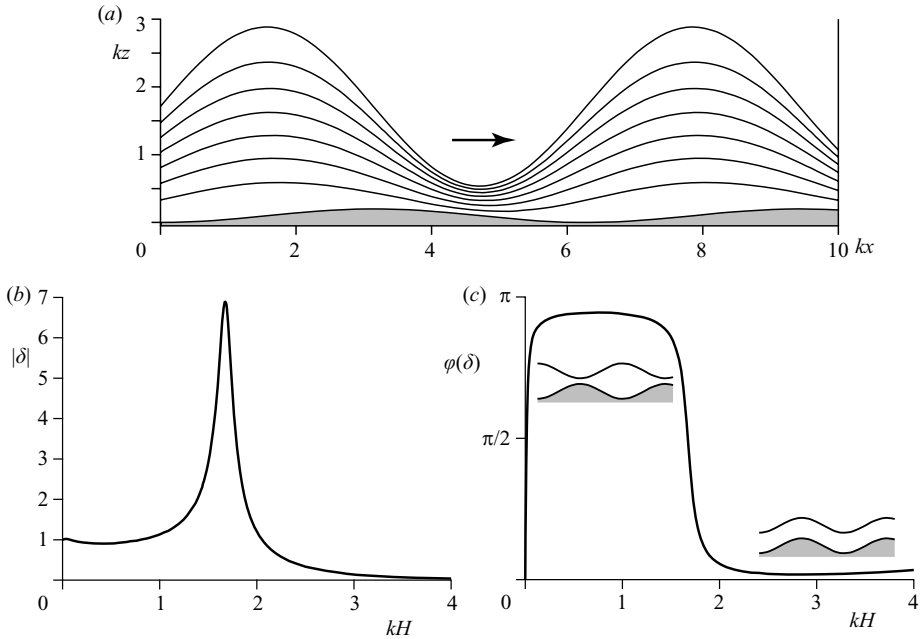$$\mathscr{F} = \sqrt{\frac{\tanh(kH)}{kH}}. \qquad (2.69)$$

FIGURE 7. (*a*) Streamlines of a flow over a sinusoidal bottom close to the free-surface resonance conditions ($\varphi = \pi/2$). The flow is from left to right. Note the squeezing of the lines *downstream* of the crest of the bump. Amplitude $|\delta|$ (*b*) and phase $\varphi(\delta)$ (*c*) of the free surface as a function of kH for $\mathscr{F} = 0.8$. The peak in amplitude and the phase shift from 0 to π correspond to the resonance. The two schematics illustrate the situations in phase or in antiphase.

In the shallow-water approximation ($kH \ll 1$), this resonant condition gives $\mathscr{F} = 1$ as standardly obtained in hydraulics. In the deep water approximation, it gives $\mathscr{F} = 1/\sqrt{kH}$ or equivalently $kH = 1/\mathscr{F}^2$ (Kennedy 1963). Consequently, the flow is subcritical *with respect to the wavelength* λ at low $\mathscr{F}$ and low kH and supercritical at large $\mathscr{F}$ and kH. Ignoring dissipation, the Bernoulli relation states that the sum of the gravitational potential energy $\rho g \Delta$ and the kinetic energy $(1/2)\rho u_{surface}^2$ is constant along the free surface. The subcritical regime corresponds to deep slow flows dominated by gravity: as the velocity increases over a bump, the corresponding increase of kinetic energy must be balanced by a loss of gravitational potential energy. As a consequence, the free surface is pinched over the bump ($\varphi = \pi$; see figure 7*c*). The supercritical regime corresponds to thin rapid flows dominated by kinetic energy. By conservation of the flow rate, a pinch of the free surface would lead to an increased velocity. As the bump pushes up the free surface, the corresponding gain of potential energy should be balanced by a decrease of kinetic energy which is achieved by a deformation of the free surface in phase with the bump ($\varphi = 0$; see figure 7*c*). In summary, the free surface responds in phase with the excitation at small wavelength and becomes delayed as λ/H increases. As in a standard second-order linear system, the disturbance and the system response are in quadrature at the resonance.

The phase φ and the rescaled amplitude $|\delta|$ of the free surface are displayed in figure 8(*a*, *b*) for different values of $\mathscr{F}$. One can see that the amplitude of the resonance increases with the Froude number. For very small $\mathscr{F}$, the phase curve is more complicated to interpret, but note that this corresponds to a vanishing amplitude δ: the resonance essentially disappears. For $kH \to 0$, one recovers the predictions
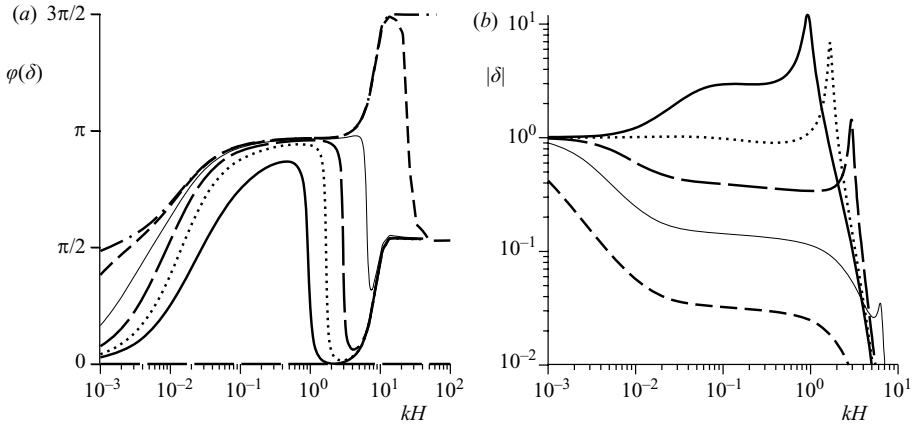
FIGURE 8. The phase (*a*) and amplitude (*b*) of the rescaled free surface deformation $\delta = \Delta/\zeta$ as a function of kH for $\mathscr{F} \rightarrow 0$ (dotted dashed line), $\mathscr{F} = 0.2$ (dashed line), $\mathscr{F} = 0.4$ (thin solid line), $\mathscr{F} = 0.6$ (long dashed line), $\mathscr{F} = 0.8$ (dotted line) and $\mathscr{F} = 1$ (solid line), and $H/z_0 = 10^3$. Crossing the resonance, the phase shifts from 0 to π.
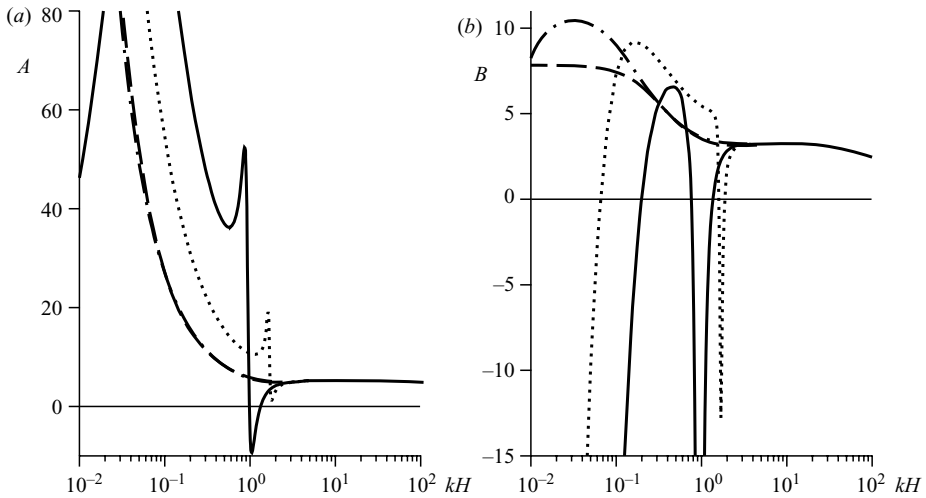

FIGURE 9. A and B as functions of kH, for $\mathscr{F} = 0.1$ (dotted dashed line), $\mathscr{F} = 0.8$ (dotted line) and $\mathscr{F} = 1$ (solid line). The dashed lines correspond to a rigid boundary at the same height H. The plots have been computed for $H/z_0 = 10^3$. Comparing a free surface to a rigid boundary condition (or to the case $H \ll \lambda$), it can be inferred that the hydrodynamics is controlled by the surface waves. In particular, the resonance leads to a drop of the shear stress component B, i.e. to a downstream shift of the point of maximum shear stress.

of Saint-Venant equations: the pressure horizontal gradient becomes much smaller than the shear stress vertical gradient so that the free surface follows the bottom topography ($\delta = 1$, $\varphi = 0$).

The basal shear stress and pressure and subsequently the coefficients A and B are modified by the presence of the free surface when kH is of order one and below. In figure 9, the coefficients are plotted as functions of kH for different values of the Froude number. One can see that the resonance peak is more pronounced for larger $\mathscr{F}$ – they are actually not visible when $\mathscr{F}$ is too small. In agreement with the

streamlines of figure 7(*a*), which shows a squeezing downstream of the bump crest, the peak of *B* is negative, corresponding to a phase delay of the stress with respect to the bottom. Furthermore, the curves corresponding to the presence of a rigid lid at the same height *H* do not exhibit these peaks. Finally, the large negative values of *B* as $kH \to 0$ also result from a free surface effect as, in the same limit, *B* reaches a positive plateau in the case of a rigid top boundary. In this limit, inertial effects become negligible and the flow is at equilibrium between gravity and friction. As a consequence, the basal shear stress is asymptotically in quadrature with the relief ($B < 0$ and $A \to 0$).

As a conclusion, there are two situations in which the excitation of standing waves by the topography affects significantly the characteristics of the inner layer: (i) around the resonance, since the surface wave amplitude is very large and (ii) for vanishing kH, when the distance *H* between the topography and the free surface becomes so small that the inner layer invades the whole flow.

3. Primary linear instability: subaqueous ripples

3.1. *Sediment transport: the saturation length paradigm*

The different modes of sediment transport by a fluid (bed load, saltation, reptation, sheet flow and suspended load) and the different dynamical mechanisms controlling this transport (hydrodynamical erosion of the bed, splash, mixing by turbulent fluctuations, etc.) can be described in a common general framework with only few key variables. The reference situation is a uniform turbulent boundary layer of constant shear velocity u_* over a flat sand bed characterized by a threshold shear velocity u_{th}. In this situation, one observes a steady uniform transport characterized by a flux q_{sat} called the saturated flux, which corresponds to an equilibrium state between flow and transport. Note that q_{sat} is a function of u_* and u_{th}. Considering a heterogeneous situation – for instance a spatial variation of the shear stress – the sand flux is not instantaneously in equilibrium with the local shear stress. In most of the situations, the transient towards equilibrium can be described by a first-order relaxation law, with a single time and length scales:

$$T_{sat}\partial_t q + L_{sat}\partial_x q = q_{sat} - q, \tag{3.1}$$

where the flow goes in the increasing *x* direction. In a situation homogeneous in space, T_{sat} is the time needed for the flux to reach saturation if the flow speed suddenly changes. Conversely, in a steady situation where there is no sediment flux at the entrance of a volume of control, L_{sat} is the length needed for the flux to reach q_{sat}. As the relaxation time is usually much smaller than the time scale of evolution of the bedform, we are left with a description of the transport by three variables: the saturated flux q_{sat}, the threshold shear velocity u_{th} and the saturation length L_{sat}. Note, in particular, that gravity effects are included into the transport threshold. This multi-scale approach allows us to separate clearly the dynamical mechanisms that govern the emergence of bedforms from those governing sediment transport. This framework lies on two important assumptions. First, the depth of the inner layer in which the shear stress is vertically homogeneous should always remain larger than the depth of the transport layer. Second, there is in general more than one relaxation mode and, consequently, a whole spectrum of relaxation times and lengths. The description by a first-order relaxation implies that one of these modes is significantly slower than (and thus dominant in front of) the others. Otherwise, two

or more saturation lengths have to be taken into account in a higher-order relaxation equation.

The subaqueous sediment transport presents four regimes (see the review by Andreotti 2009).

(i) *Erosion limited regime.* Close to the threshold, only a small fraction of the grains at the surface is entrained and this erosion process takes some time to occur. The concentration of mobile grains is not sufficient to induce a significant reduction of the flow strength. The grains transported in this dilute situation are isolated from each other. The transport reaches equilibrium when deposition balances erosion (Charru, Mouilleron-Arnould & Eiff 2004). The saturated flux is controlled by the erosion time and the disorder of the bed. The saturation length L_{sat} is then the mean length of the trajectory of one grain between two trapped states. We introduce the fraction $\mathcal{N}(\Theta)$ of grains at the surface susceptible to be entrained at a Shields number Θ, which reflects and encodes the distribution of potential wells at the sand bed surface. In the absence of flow, for $\Theta = 0$, $\mathcal{N}$ is null. It increases very quickly around the mean threshold Shields number Θ_{th} and reaches 1 at a second threshold Θ_M. The mean area explored by the grain is $L_{sat}d$ and contains, by definition, a mean number of potential wells sufficiently deep to trap the grain equal to 1. We then obtain the expression of the saturation length:

$$L_{sat} = \frac{d}{1 - \mathcal{N}(\Theta)}. \tag{3.2}$$

Here, L_{sat} is equal to one grain diameter d at Θ_{th} and diverges at Θ_M. This divergence has been directly evidenced experimentally in the viscous case by Charru *et al.* (2008).

(ii) *Suspended regime.* For sufficiently small grains, at larger Shields numbers, the turbulent velocity fluctuations become dominant as they induce drag force fluctuations on the order of gravity. In such a turbulent suspension, the feedback of sediment transport on the flow may still be neglected. The transport reaches equilibrium due to the finite thickness H of the flow, when the sedimentation flux balances the upward turbulent diffusion flux. In rivers, at moderate Froude numbers, ripples and dunes are composed of grains sufficiently heavy to prevent suspension.

(iii) *Momentum limited regime.* For sufficiently large grains, the erosion-limited regime is left at moderate Shields numbers for a regime in which the transport becomes limited by the available momentum: each time the flow entrains a grain from the bed and accelerates it, this grain exerts in turn a stress on the fluid. The transition from erosion to momentum limited regimes takes place below Θ_M, when the concentration of transported grains becomes important. Saturation is reached when the fluid-borne basal shear stress has been so much reduced that deposition balances erosion. The saturation length is then given by the length needed by the grain to reach its asymptotic velocity – the so-called drag length. The modelling of the drag length is a difficult problem as the trajectory takes place in a turbulent flow whose fluctuations are *not* due to the motion of the grain itself. The problem is thus very different from that of a sphere moving in a fluid at rest, a problem for which the drag law is calibrated. To the best of our knowledge, the motion of a sphere whose diameter lies in the inertial range of the turbulent flow is still an open problem. We are thus left with the standard drag force formula $(\pi/8)C_d\rho_f U^2 d^2$, with a drag coefficient of order one. Then, solving the equation of motion, one obtains a drag length and thus a saturation length around:

$$L_{sat} \simeq 2\frac{\rho_s}{\rho_f}d. \tag{3.3}$$

(iv) *Sheet flow regime.* As the Shields number increases, more and more grains are transported, and one reaches a regime of dense suspension where the transport is located in a dense thick granular layer (Bagnold 1956). Saturation is still due to the negative feedback of transport on the flow. The saturation length has not yet been derived for this two-phase flow regime. As natural rivers flow at Shields numbers slightly above the threshold, the transport is usually not sufficiently dense to form a sheet flow.

Here, we adopt a convenient parametrization of the saturated flux, valid for the different transport regimes:

$$q_{sat} = \chi u_*^{2\gamma} (u_*^2 - u_{th}^2). \tag{3.4}$$

For instance, the self-consistent model derived by Andreotti (2009) for the momentum limited regime gives $\gamma = 0$, whereas the Bagnold (1956) formula involves an exponent $\gamma = 1/2$. Other empirical models such as Meyer-Peter & Müller (1948), Einstein (1950) or Yalin (1963) can also be approximated in this way.

3.2. *Linear stability analysis*

We consider a periodic disturbance of the bed profile Z. As the base state is homogeneous, we can seek for modes of the form $\exp(\sigma t + ik(x - ct))$. Taking the Fourier transform, noted with a circumflex (^), the shear stress induced by the wavy sand bed reads $u_*^2(A + iB)k\hat{Z}$. The computation of the coefficients A and B has been performed under the assumption that the sand bed is static. As a matter of fact, the growth rate σ is related to the sediment transport and is on the order of q_{sat}/L_{sat}^2. Experimentally, σ is usually found to be 4 orders of magnitude smaller than the typical flow shear rate: the time scale of formation of subaqueous ripples is typically 10 s to be compared with few tens of microseconds for the period at which the flow is excited by the dune relief, λ/U. Therefore, the normal velocity of the grain–fluid interface does significantly change the flow in this problem (Fourrière *et al.* 2009). The threshold shear stress is a function of the slope $\tan \alpha$ (Fernandez Luque & van Beek 1976; Yalin & Karahan 1979; Loiseleux *et al.* 2005; Andreotti 2009):

$$\hat{u}_{th}^\alpha = u_{th} \frac{ik\hat{Z}}{2\mu}, \tag{3.5}$$

where μ is the avalanche slope. At linear order, the saturated flux $q_{sat}(u_*, u_{th})$ reads

$$\hat{q}_{sat} = \frac{\partial q_{sat}}{\partial u_*} \frac{u_*}{2} (A + iB)k\hat{Z} + \frac{\partial q_{sat}}{\partial u_{th}} \frac{u_{th}}{2\mu} ik\hat{Z}. \tag{3.6}$$

Introducing the reference flux $Q = (\gamma + 1)\chi u_*^{2(\gamma+1)}$ the above expression takes the form

$$\hat{q}_{sat} = Q(a + ib)k\hat{Z}, \tag{3.7}$$

where a and b are the components of the saturated flux in and out of phase with the topography:

$$a = A - \frac{\gamma A}{1 + \gamma} \frac{u_{th}^2}{u_*^2} \quad \text{and} \quad b = B - \frac{\gamma B + \mu^{-1}}{1 + \gamma} \frac{u_{th}^2}{u_*^2}. \tag{3.8}$$

For asymptotically large shear stresses, i.e. $u_* \gg u_{th}$, a tends to A and b tends to B, independent of γ and μ. Close to the threshold (for $u_* \simeq u_{th}$), a tends to $A/(1 + \gamma)$ and b tends to $(B - \mu^{-1})/(1 + \gamma)$. The flux relaxes to its saturated value with a spatial lag L_{sat}:
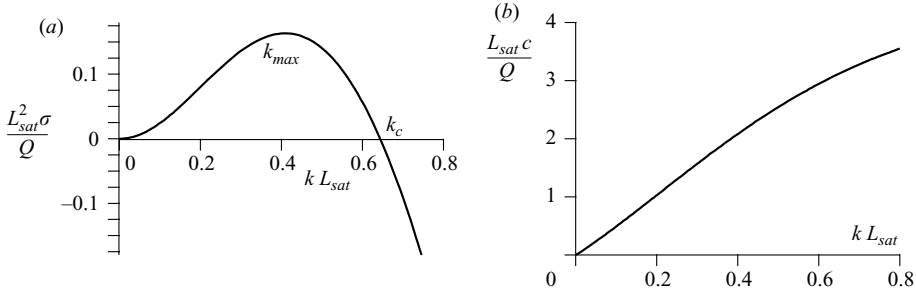
$$ikL_{sat}\hat{q} = \hat{q}_{sat} - \hat{q}. \tag{3.9}$$

FIGURE 10. Dispersion relation for $\mu = \tan 32°$ and $u_{th} \ll u_*$. (a) Growth rate σ as a function of the wavenumber rescaled by the saturation length kL_{sat}. (b) Propagation speed c and Q is the reference flux.

Using the conservation of mass $\partial_t Z + \partial_x q = 0$, one obtains the dispersion relation

$$\sigma - ikc = -ik\frac{\hat{q}}{\hat{Z}} = -\frac{ik}{1 + ikL_{sat}}\frac{\hat{q}_{sat}}{\hat{Z}} = -\frac{iQ(a + ib)k^2}{1 + ikL_{sat}}. \quad (3.10)$$

Splitting the equation into its real and imaginary parts, one obtains the growth rate σ and the propagation speed c:

$$\frac{L_{sat}^2\sigma}{Q} = \frac{(kL_{sat})^2(b - akL_{sat})}{1 + (kL_{sat})^2}, \quad (3.11)$$

$$\frac{L_{sat}c}{Q} = \frac{(kL_{sat})(a + bkL_{sat})}{1 + (kL_{sat})^2}. \quad (3.12)$$

This corresponds to a standard convective instability at large wavelengths (figure 10). The cutoff wavenumber k_c above which modes are stabilized by the saturation length is given by

$$k_c L_{sat} = \frac{b}{a}. \quad (3.13)$$

Note that the instability can present a different threshold than that for the transport if b vanishes at some value of u_* larger than u_{th}, i.e. if B is smaller than μ^{-1}. In the first approximation, a and b are weak functions of kz_0. Then, one can approximate the maximum growth rate wavenumber k_{max} as

$$k_{max}\, L_{sat} \simeq X^{-1/3} - X^{1/3} \quad \text{with} \quad X = -\frac{b}{a} + \sqrt{1 + \left(\frac{b}{a}\right)^2}. \quad (3.14)$$

As the instability is convective, we have also computed the spatial growth rate. Its maximum nicely coincides with that of the time growth rate.

It can be inferred from the conservation of mass that the propagation velocity c is proportional to the difference of flux δq between trough and crest and inversely proportional to the ripple height 2ζ – this is the so-called Bagnold relation in the aeolian context. At large wavelength λ, δq is proportional to the reference flux Q and to the height so that the propagation speed varies as $c \propto Q/\lambda$. This is confirmed by figure 10(b), which shows a roughly linear relation between c and k.

3.3. Ripples wavelength selection

The fastest growing wavelength λ_{max} can be computed, taking into account the dependencies of A and B on kz_0. There are two length scales in the problem: z_0,
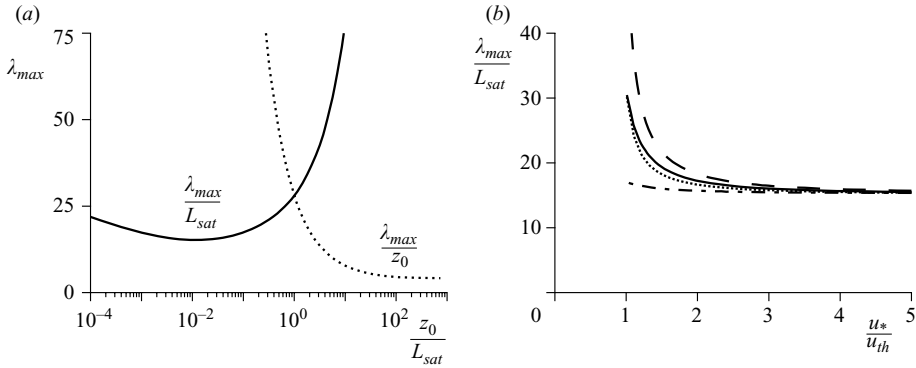
FIGURE 11. (*a*) Wavelength λ_{max} of maximum growth rate as a function of the ratio of the two characteristic length scales z_0/L_{sat}, in the limit $u_* \gg u_{th}$, for $\mu = \tan 32°$ and $\gamma = 0$. Solid line: ratio λ_{max}/L_{sat}. Dotted line: ratio λ_{max}/z_0. (*b*) Wavelength λ_{max} rescaled by L_{sat} as a function of the rescaled shear velocity u_*/u_{th} for $L_{sat}/z_0 = 80$ (typical subaqueous case with sand grains). The curves correspond to $\mu = \tan 32°$ and $\gamma = 0$ (solid line), to $\mu = \tan 32°$ and $\gamma = 1/2$ (dotted line), to $\mu = \tan 24°$ and $\gamma = 0$ (dashed line) and to $\mu = \tan 70°$ and $\gamma = 0$ (dot–dashed line).

which is an hydrodynamical quantity, and L_{sat}, which is related to the sand transport. Figure 11 shows that the saturation length controls the scaling of λ_{max} if L_{sat} is larger than z_0. In this case, the wavelength is the product of a non-dimensional prefactor of hydrodynamical origin (function of b/a; see (3.14)) by the transport saturation length. Conversely, z_0 controls the scaling of λ_{max} if it is larger than $10\,L_{sat}$. In this case, the maximum growth rate is directly related to the maximum of the function $B(kz_0)$ (figure 4*b*). This could be the case in the hydraulically smooth regime for which z_0 scales on ν/u_* (Sumer & Bakioglu 1984). For subaqueous ripples, the measurements of initial wavelength are usually larger than $100\,d$, whereas z_0 is on the order of $0.1\,d$. If the scaling was controlled by z_0, one would underestimate the most unstable wavelength by 2 orders of magnitude. As a consequence, the wavelength scales on the transport saturation length L_{sat}. This means that models in which the flux is a function of the shear stress cannot capture correctly the physics of ripple instability. The second conclusion is that, although the saturation length may be determined by different dynamical mechanisms, aeolian dunes are of the same nature as subaqueous ripples. In other words, different modes of sediment transport (e.g. saltation and reptation bed load) in different situations (e.g. viscous and turbulent) can lead to bedforms instabilities of same nature (see Hersen, Douady & Andreotti 2002; Charru 2006; Claudin & Andreotti 2006). Note that aeolian ripples do not belong to the same class of bedforms as they result from a screening instability (Bagnold 1941; Anderson 1987, 1990; Andreotti, Claudin & Pouliquen 2006), not from a hydrodynamical instability.

Figure 11(*b*) shows that the transport model has a negligible influence on the selected wavelength. This indicates that L_{sat} and q_{sat} are the single two relevant quantities encoding the sediment transport details. Because of the stabilizing role of gravity encoded in the slope dependence of the threshold, λ_{max} increases close to the threshold shear stress. Of course, this effect is very sensitive to the value of μ, as shown in figure 11(*b*). For natural sand grains ($\mu = \tan 32°$), the wavelength λ_{max} decreases from $30\,L_{sat}$ at the threshold to $20\,L_{sat}$ far from it. For glass beads, the prediction is very different depending whether one takes the avalanche slope ($\mu = \tan 24°$) or the experimental data of Loiseleux *et al.* (2005) (equivalent to a fictitious $\mu = \tan 70°$)
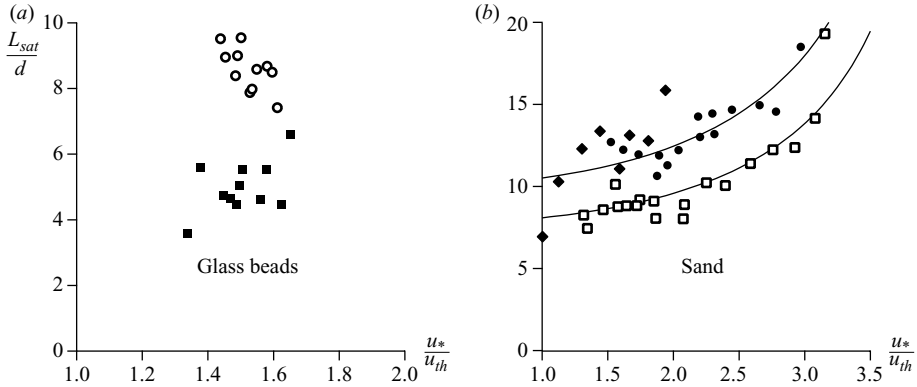
FIGURE 12. Saturation length in water determined from experimental measurements of the initial wavelength as a function of the shear velocity for different types of particles. (*a*) Glass beads (Langlois & Valance 2007): $d = 250\ \mu m$ ($\circ$) and $d = 500\ \mu m$ ($\blacksquare$). (*b*) Natural sand grains (Coleman & Melville 1996 and Baas 1999): $d = 210\ \mu m$ ($\bullet$), $240\ \mu m$ ($\blacklozenge$), $d = 830\ \mu m$ ($\square$). The solid lines correspond to the best fit of (3.2). These curves tend to diverge for $u_* = u_M \simeq 4.5\ u_{th}$ or equivalently for $\Theta = \Theta_M \simeq 20\ \Theta_{th}$. In (*a*) and (*b*), the small factor between small and large grains could be due to a subdominant dependence of L_{sat} on viscosity.

for the slope effect. In the latter case, λ_{max} is almost independent of u_* whereas it diverges at the threshold in the former case as B is then of the order of $1/\mu$.

3.4. *Comparison with experiments*

Rather than predicting the wavelength and comparing it with experimental data, we can invert the process and determine the value of the saturation length that would give the observed wavelength. This allows us to remove the dependence of the wavelength with respect to u_* due to the slope effect. For this, μ is taken equal to the avalanche slope. Most of the experimental data available in the literature correspond to well-developed ripples. As these bedforms exhibit pattern coarsening, it is very important to focus on papers reporting the initial wavelength (linear regime), measured for grain sizes larger than 200 μm (hydraulically rough sand bed). We have selected five such data sets (Coleman & Melville 1996; Baas 1999; Langlois & Valance 2007).

As shown in figure 12, they present consistent trends, which is not the case for the data obtained with smaller grains ($d \sim 100\ \mu m$). The saturation length is found to be on the order of several grain diameters. It is slightly smaller for the glass bead experiments than that for the natural sand grain ones. The data points around the threshold are very sensitive to the values taken for μ and u_{th} in the model and should not be overinterpreted. The slight increase of L_{sat} with u_* is more robust, although it is based on the last few data points. More significant is the decrease of the ratio L_{sat}/d when d increases, a feature present for both glass beads and sand grains. It could be related to a subdominant dependence on viscosity.

We have discussed above the two simplest possibilities for the dynamical mechanisms limiting the transport saturation: erosion and inertia. Concerning erosion, the prediction $L_{sat} \propto d/(1 - \mathcal{N}(\Theta))$ is almost impossible to verify as the distribution of potential wells at the surface of the bed is not known. Still, with the simple parametrization chosen above, one expects the saturation length to scale on the grain size and to gently increase with u_*. The solid line in figure 12(*b*) is the best fit by such a form. One obtains the estimate $\Theta_M/\Theta_{th} \sim 20$. This value is far above the ratio around 2 that has been found experimentally by Charru *et al.* (2008). It means that
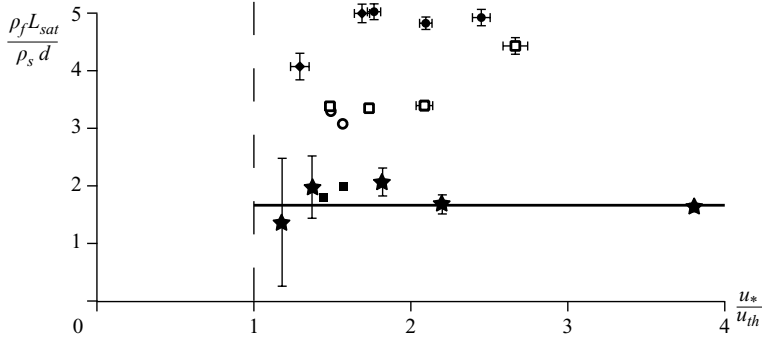
FIGURE 13. Comparison between the saturation length, rescaled by $(\rho_s/\rho_f)\,d$, in the aeolian ($\bigstar$) and subaqueous (other symbols; see figure 12) cases. For aeolian dunes, L_{sat} is determined from the most unstable wavelength under well-characterized winds (Andreotti, Claudin & Pouliquen 2009). For subaqueous ripples, each point of this graph corresponds to the very same data as in figure 12, but averaged over six measurements. The dashed line corresponds to the entrainment threshold. The solid line is the average over the different points measured in the aeolian case: $L_{sat} \simeq 1.66\,(\rho_s/\rho_f)\,d$.

the erosion length is probably not the mechanism limiting saturation. Otherwise, one would expect a much more rapid increase of the saturation length. Instead, one can observe that it is almost constant, with a subdominant, slow increase with u_*.

Figure 13 aims to test the second simple possibility: an inertia-limited saturation length. In this case, one expects a scaling law of the form $L_{sat} \propto (\rho_s/\rho_f)\,d$ similar to that observed for aeolian sand transport (Hersen *et al.* 2002; Andreotti 2004; Claudin & Andreotti 2006; Andreotti & Claudin 2007). We have used the measurements of the wavelength at which aeolian dunes form reported in Andreotti *et al.* (2009), obtained either in the field or using aerial photographs. Using the inversion method proposed here, the saturation length L_{sat} has been obtained for different values of the wind shear velocity (figure 13) and is mostly independent of it. Once rescaled by $\rho_s/\rho_f\,d$, L_{sat} is of the same order of magnitude for both aeolian dunes and subaqueous ripples. In the first approximation, all series of data, considered separately, are independent of u_*. A better agreement with aeolian data is observed for glass beads and large grains. A discrepancy by a factor of two is observed for small natural sand grains. As a possible interpretation, the grains roll on the ground during their phase of acceleration, which may lead to underestimate the length needed to reach the fluid velocity. One expects rough sand grains to be more sensitive to this effect.

4. Effect of the free surface

4.1. *Dispersion relation*

In the previous section, both hydrodynamic and erosion aspects have been gathered to study bedforms under an infinite depth assumption, i.e. ripples. However, rivers have a free surface at a finite height H. We expect these additional ingredients to significantly change the shape of the dispersion relation. We have computed above the basal shear stress coefficients (A and B) in that case (figure 5). The large wavenumbers are insensitive to the free surface. By contrast, A and B display a resonance peak around $kH \simeq 1/\mathscr{F}^2$ and have a divergent behaviour as $k \to 0$. As σ and c are directly related to A and B through (3.11) and (3.12), they both present the same features. In figure 14(*a*), the growth rate is represented as a function of kz_0 for three different
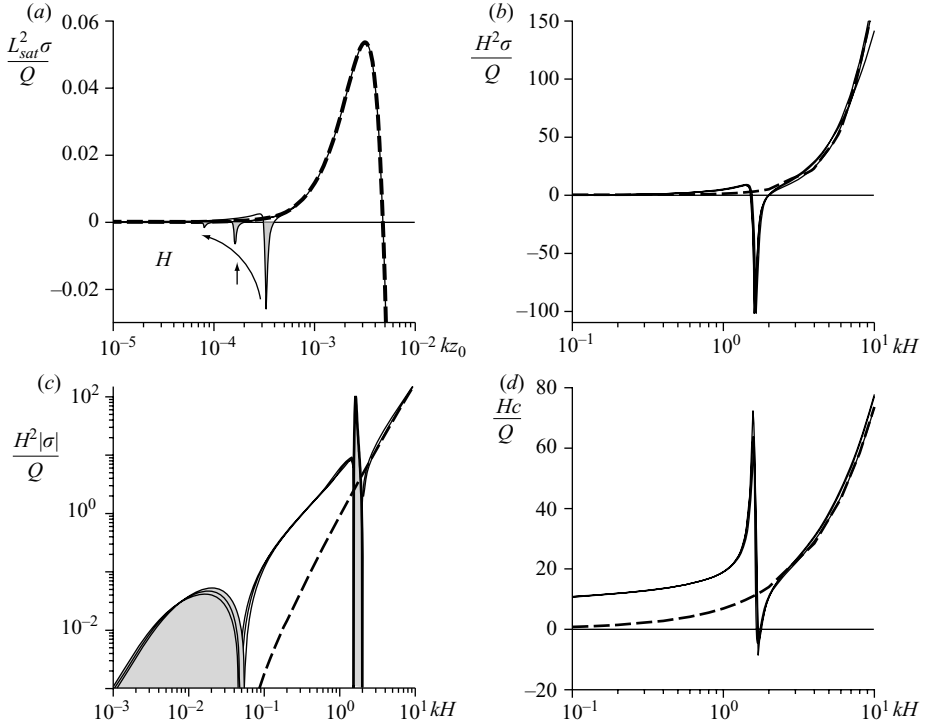
FIGURE 14. Growth rate σ and propagation velocity c as functions of the wavenumber k for different values of H/z_0 ($H/z_0 = 5000, 10\,000, 20\,000$) and the typical values of parameter $\mathcal{F} = 0.8$, $\mu = \tan 32°$, $u_{th}/u_* = 0.8$ and $L_{sat}/z_0 = 80$. In (a), σ is rescaled by L_{sat} and k by z_0, whereas in (b–d) all lengths are rescaled by the relevant length scale H, so that all curves collapse in region where $kH \simeq 1$. The dashed line represents the reference unbounded case presented in the previous section. In (c), because of the log scale, the absolute value of σ is displayed and the grey areas encode for negative values of the growth rate.

values of H/z_0. All curves collapse in the large-k region on the dispersion relation computed in the reference unbounded case. In particular, they exhibit a maximum for the same wavenumber, which corresponds to the initial ripple wavelength. This means that the presence of the free surface does not influence the formation of ripples as long as H and L_{sat} are well-separated length scales. In a zone around $kH \simeq 1/\mathcal{F}^2$ (figure 14b), the function $\sigma(k)$ presents, in comparison to the reference unbounded case, a sharp dip that can be attributed to the resonance of gravity surface waves. As shown in figure 15(a), the width and the amplitude of this dip is very sensitive to the value of the Froude number. For small $\mathcal{F}$, the effect of the resonance is marginal and the dip is very small. As the Froude number increases, the dip becomes more pronounced so that the growth rate σ becomes negative in an enlarging range of wavenumbers: the free surface stabilizes wavelengths commensurable with the flow depth. Last, the semi-logarithmic plot of figure 14(c) reveals the behaviour of the growth rate in the small-kH limit: $\sigma(k)$ tends to 0 from below. This indicates that the very large wavelengths are also stabilized. In the intermediate range of wavelengths, a slight increase of the growth rate is observed. The other output of the linear stability analysis is the propagation velocity of the pattern $c(k)$ (figure 14d), which is also very sensitive to the resonance at $kH \simeq 1/\mathcal{F}^2$. It presents a sharp maximum on the left of
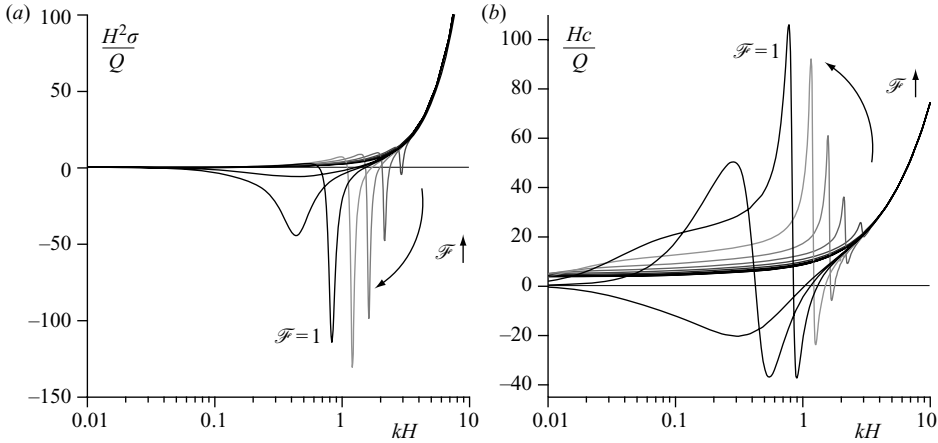
FIGURE 15. Dispersion relation obtained for a ratio $H/z_0 = 10\,000$, $\mu = \tan 32°$, $u_{th}/u_* = 0.8$ and $L_{sat}/z_0 = 80$. (a) Growth rate σ as a function of the wavenumber for different values of the Froude number. (b) Propagation speed c. In (a, b), the Froude number $\mathscr{F}$ is varied from 0.5 to 1.2 by increment of 0.1.
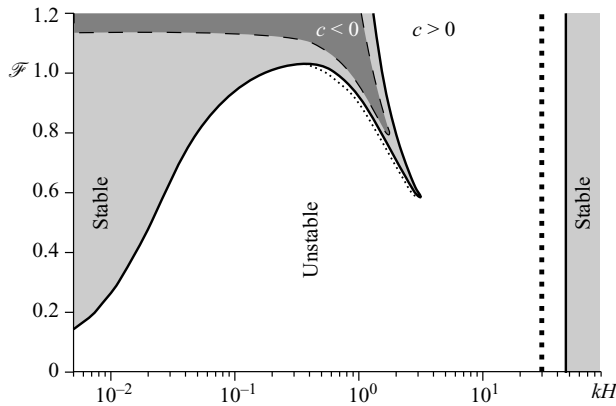

FIGURE 16. Stability diagram parametrized by the Froude number $\mathscr{F}$ and the rescaled wavenumber kH. The marginal stability curves ($\sigma = 0$), shown in solid lines, separates the unstable zone (white) from the stable ones (grey). The overall maximum growth rate (bold dotted line) is always reached for ripples. The local maximum of the growth rate resulting from the resonance of standing surface waves is shown by the thin dotted line. The dashed line ($c = 0$) separates upstream ($c < 0$, dark grey) from downstream propagating bedforms. The other parameters are set to $H/z_0 = 10\,000$, $\mu = \tan 32°$, $u_{th}/u_* = 0.8$ and $L_{sat}/z_0 = 80$.

the resonance followed by a dip on the right of it. At this dip, c can become negative for sufficiently large Froude numbers ($\mathscr{F} \gtrsim 0.7$).

4.2. *Dune formation*

Gathering the different dispersion relations in the ($\mathscr{F}, kH$) space, one produces the stability diagram (figure 16). The central region delimited by the two marginal stability curves corresponds to the zone of unstable wavelengths ($\sigma > 0$). Large k are stabilized by the saturation length, which explains the lack of dependence on the Froude number in this zone: both the marginal stability and the maximum growth rate curves are vertical lines in the diagram. This simply reflects the fact that ripples do not feel the

free surface: they disturb the flow over a thickness of the order of the wavelength λ, i.e. much smaller than H. As already mentioned, the most unstable mode always corresponds to ripples (dotted vertical line in the large-k zone of figure 16).

A second zone of stable modes is located around the resonant conditions, when the surface wave amplitude reaches a maximum (figure 7b). The waves are in phase for wavenumbers above the resonance and in antiphase below it (figure 7c). At the resonance, the free surface is in quadrature with the bottom, which tends to move downstream the point of maximum shear stress, i.e. to stabilize the bedform. Of course, as the influence of the free surface on the flow is localized over a typical distance λ, its effect is more important as kH becomes smaller. In summary, there are two conditions under which the free surface can overcome the inertial destabilizing effect: (i) around the resonance, because the standing wave amplitude is very large and (ii) in the limit of small wavenumbers, as H becomes much smaller than wavelength λ. It can be observed in figure 16 that a sharp stable zone surrounds the resonant curve. For obvious reasons, this new minimum of the growth rate associated with the surface wave resonance comes with a local maximum of σ (thin dotted line along the re-stabilized zone). In the work of Richards (1980), the latter has been associated with the formation of dunes by a linear instability. In many other linear analyses, the prediction of ripples is missed – the corresponding maximum in the dispersion relation is absent – either because the inner layer responsible is not described (Kennedy 1963; Reynolds 1965; Engelund 1970; Fredsøe 1974; Coleman & Fenton 2000) or because the sediment transport is not correctly described (Colombini 2004; Colombini & Stocchino 2005). As a consequence, they are left with a unique peak in the region of kH around unity, which is found here to be a secondary maximum. As explained below, we fundamentally disagree with the conclusion reached in all these papers that subaqueous dunes result from the linear instability of a flat bed.

Let us briefly recall the basic reasons for which one usually associates the appearance of a pattern to a maximum of the growth rate. One considers that the initial condition $Z(t = 0)$ is essentially flat, with some wide-band noise. Its Fourier transform $\hat{Z}(k, t = 0)$ then contains some energy in a wide range of wavenumbers k. In the linear regime, the surface profile reads

$$\hat{Z}(k, t) = \hat{Z}(k, t = 0)e^{\sigma(k)t}. \tag{4.1}$$

If the distribution of initial amplitude is initially sufficiently flat and if the growth rate $\sigma(k)$ presents a sharp *absolute* maximum in k_{max}, then a pattern dominated by the corresponding wavelength λ_{max} emerges, as this mode grows the fastest. In the present case, the amplitude of this secondary maximum close to the resonance is almost the same as the value of σ at the same wavenumber in the unbounded case. Moreover, most of the modes between the resonance and the ripple peak are in fact much more unstable: if a linear instability could be invoked, the amplitude of all these intermediate modes would eventually be larger than that of this local maximum. Furthermore, the ratio of the primary and the secondary maxima of the growth rate is on the order of $(H/L_{sat})^2$, which is a large number: it is typically on the order of 10^4 for flume or small river experiments ($d \simeq 400\ \mu m$ and $H \simeq 40$ cm) and 10^6 for a large river ($d \simeq 400\ \mu m$ and $H \simeq 4$ m). For example, taking half a minute for the characteristic ripple apparition time (figure 17a), it would give ~ 3 days for the dune linear growth time scale, i.e. much too large in comparison to observations (figure 18). For these reasons, this secondary peak in the dispersion relation cannot be associated with dunes.
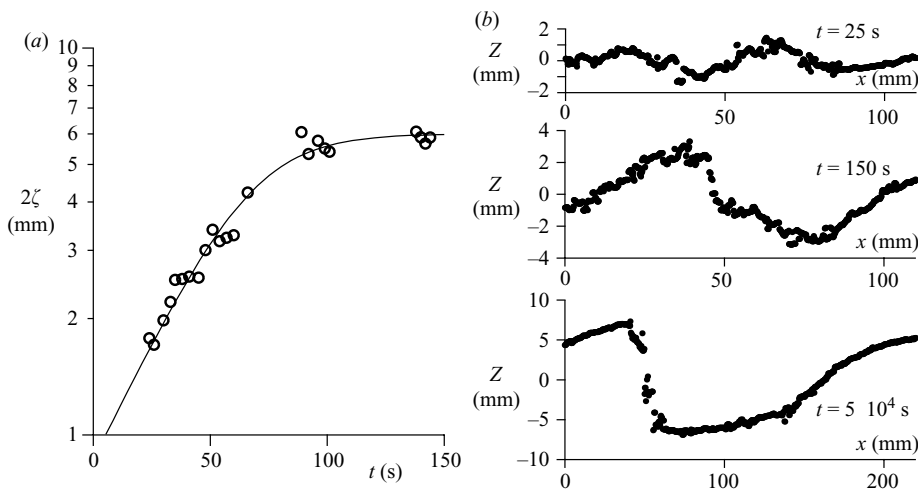
FIGURE 17. Formation of ripples in a natural river, starting at $t = 0$ from a flat sand bed. The experiment was performed in the Leyre river, at Sauniac bridge, on 16 September 2008, for $H = 52$ cm, $\mathscr{F} = 0.21$ and $u_* = 3$ cm s^{-1}. The sediment is well sorted with a mean grain size $d = 320 \pm 70$ μm. (*a*) Amplitude 2ζ of the bed disturbances as function of time t. Here, ζ is determined from the auto-correlation of the bed profile $Z(x, t)$. The solid line is the best fit by (5.2) and gives $\sigma = 3 \times 10^{-2}$ s^{-1} or equivalently $\sigma^{-1} = 35$ s. (*b*) Bed elevation profile measured by taking a picture of the bed enlightened by an inclined laser sheet. Low amplitude ripples can be detected from $t = 25$ s after flattening the sand bed. Nonlinear effects make the amplitude saturate around $t = 100$ s and a clear avalanche slip face can be observed at $t = 150$ s. During this linear stage, the wavelength $\lambda \sim 90$ mm does not evolve significantly (figure 18*b*). Beyond this initial phase, a pattern coarsening towards dunes is observed, which saturates at $\lambda \simeq 20$ cm and $\zeta = 4.5$ mm after typically 1 h: tracking the pattern during further ~ 14 h, we did not observe any significant change of these characteristics.

Let us contrast this subaqueous situation to that of aeolian ripples superimposed on aeolian dunes. As already mentioned, the instability mechanism of these dunes is of the same hydrodynamics nature as that of subaqueous ripples, i.e. it comes from the upwind shift of the basal shear stress with respect to relief. Aeolian ripples, however, are generated by a screening instability: the upwind face of ripples receives more impacts of saltating grains than the downwind face (Bagnold 1941; Anderson 1987, 1990). Rapidly, nonlinearities make the ripple pattern saturate to a wavelength much smaller than that at which dunes emerge, and this saturation is faster than the dune time formation. One can then consider that dunes result from the linear instability of a flat bed that presents saturated aeolian ripples. Moreover, the growth rate at the wavelength of ripples in the dune instability is negative, because ripples are smaller than the aeolian saturation length. Conversely, the growth rate at the wavelength of dunes in the ripple instability is much smaller than the growth rate at the same wavelength in the dune instability. In conclusion, aeolian ripples and aeolian dunes can truly be associated with two different linear instabilities. In the case of subaqueous ripples and dunes, none of these criteria (different destabilizing mechanisms, saturation of ripples wavelength, separation of the modes by several decades of almost non-growing wavelengths) is fulfilled.

5. Field experiments

In this last section, we present direct experimental evidences that river dunes do not form by a linear instability. We will discuss our field measurements in the light
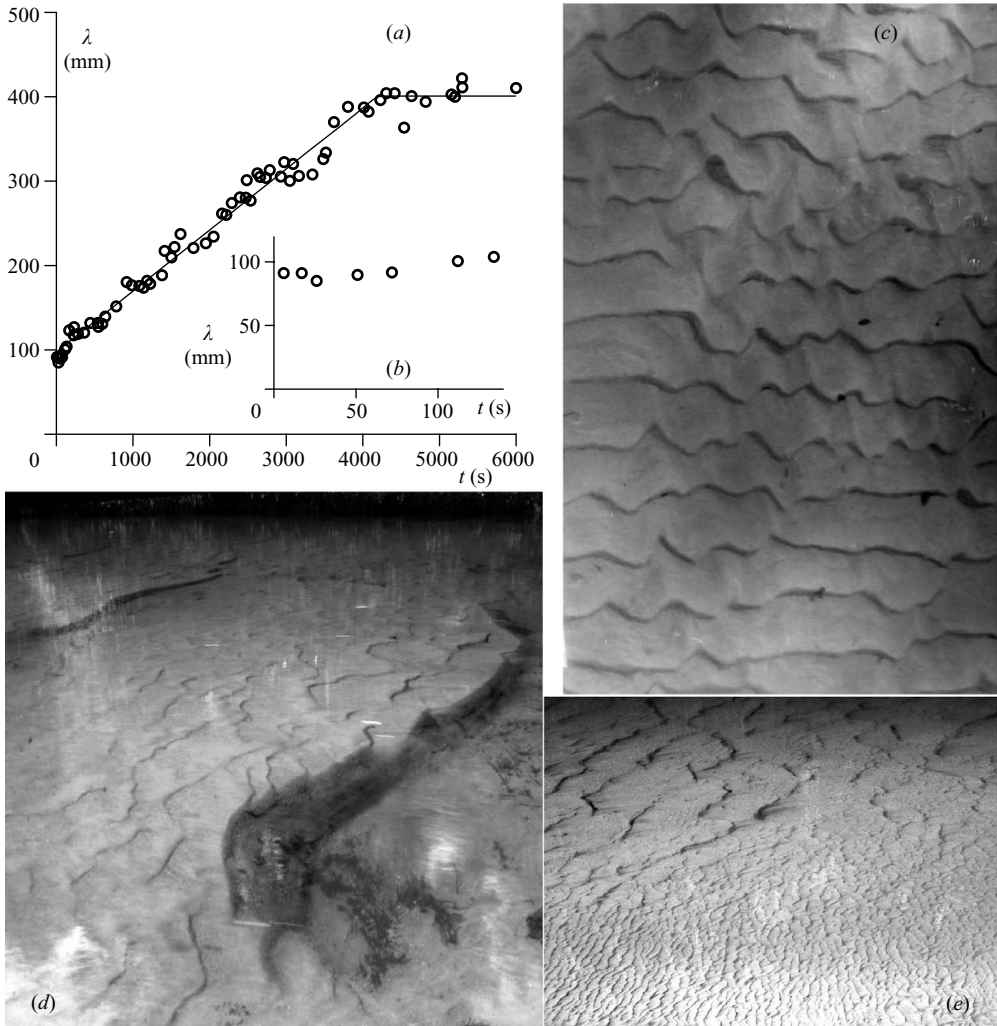
FIGURE 18. (*a–c*) Formation of dunes in a natural river, starting at $t = 0$ from a flat sand bed. The experiment was performed in the Leyre river, at Mios bridge, on 17 September 2008, for $H = 50$ cm, $\mathscr{F} = 0.28$ and $u_* = 4$ cm s^{-1}. The grain size is $d = 330 \pm 70$ μm. (*a*) Time evolution of the wavelength λ. The pattern coarsening starts after 150 s and stops after ~ 4000 s. (*b*) Same graph, but restricted to the linear regime (between $t = 0$ and $t = 150$ s). (*c*) The photograph shows the dunes of wavelength 40 cm formed after 6000 s. (*d*) Formation of mega-dunes, starting from a flat sand bed. The experiment was performed in the Leyre river, at Mios bridge, for $H = 44$ cm, $\mathscr{F} = 0.30$ and $u_* = 4$ cm s^{-1}. The sand is polydisperse: it is a mixture of sand grains of size $\sim 330 \pm 70$ μm, which cover 60 % of the surface, and of coarse grains larger than 600 μm, which represent 40 % of the surface – but 9 % of the grains and 60 % of the mass. The photograph shows 3 m long mega-dunes with ~ 40 cm superimposed dunes. (*e*) Photograph of the Leyre river at Mios bridge showing the sharp transition between dunes (zone of medium sand) and mega-dunes (zone of medium and coarse sand mixed).

of the model proposed here and show reciprocally that all existing observations are consistent with this model. We will finally propose a new definition of the different subaqueous bedforms, based on the physical mechanisms that control their formation.

5.1. *Formation of ripples*

We have studied the formation of ripples, dunes and mega-dunes in the Leyre river. This river is located in the southwest of France, in a region called 'les Landes de Gascogne' (44°32′N, 0°52′W). It flows in a particularly homogeneous basin, both in terms of the nature of the ground (rather sorted sand grains) and of the vegetation. Except during flooding events, bed load is the dominant mode of transport. The size of the grains on the river bed is around $d = 330$ μm. The experiments have been performed at the end of summer (low water period) in two straight and flat portions of the river.

The experiments were conducted as follows. Using long parallel metallic bars, the surface of the sand bed was carefully levelled at time $t = 0$, and the formation of bedforms was directly observed. In order to measure the emergence of ripples, we used a (water proof) laser sheet inclined at a low angle to the horizontal. Taking pictures through a glass plate from the top, we have determined the height profile $Z(x, t)$ along this line as a function of time. Figure 17(*b*) shows the evolution of one such a ripple from the initial stage where it is symmetric to the time when an avalanche slip face develops. To determine the wavelength λ and the amplitude 2ζ of the ripple, we computed the auto-correlation of the profile $C(X) = \langle Z(x)Z(x + X) \rangle$. Typically, 25 s after the beginning of the experiment, C shows a secondary maximum whose position gives λ and whose amplitude gives ζ. During the first 150 s, the wavelength does not evolve much (figure 18*b*) whereas the amplitude grows and saturates (figure 17*a*). As the final amplitude is not very large compared to the grain size d (and thus the initial noise level), it is difficult to get an indubitable evidence of an exponential growth. Still, the curves we obtained are consistent with a linear regime over a factor of two in amplitude (figure 17*a*). As the first nonlinear correction to the basal shear stress at the wavenumber k goes like the cube of the aspect ratio, we expect an amplitude equation of the form

$$\frac{\mathrm{d}\zeta}{\mathrm{d}t} = \sigma \zeta \left[1 - \left(\frac{\zeta}{\zeta_\infty} \right)^2 \right], \tag{5.1}$$

whose solution is

$$\zeta = \frac{\zeta_\infty}{\sqrt{1 + \exp(-2\sigma t)}}. \tag{5.2}$$

One can see in figure 17(*a*) that the fit of this relation to the data is very good, so that observations are consistent with a formation of ripples by a linear instability saturated by nonlinear hydrodynamical effects. Importantly, the rescaled growth rate $\sigma/(ku_*)$ is around 10^{-3} and the rescaled propagation speed $\omega/(k u_*)$ is around 10^{-2}. As shown in §2, with such small dimensionless numbers, the motion of the bed can be ignored in the hydrodynamical treatment.

5.2. *Formation of dunes and mega-dunes*

We have observed the evolution of the patterns for typically 2 h after flattening the sand bed (figure 18*a*). A statistically stationary state is eventually reached, which corresponds to what was observed in the natural conditions, i.e. before the experiment (figure 18*c*). As in flume experiments (Venditti *et al.* 2005*a*,*b*; Langlois & Valance 2007), we have observed a coarsening of the ripple pattern, i.e. a progressive growth of the wavelength by merging of bedforms (Raudkivi & Witte 1990; Raudkivi 2006). Figure 17(*a*) shows that this growth is linear in time and stops when the wavelength λ becomes on the order of the flow depth H. Both these processes and the time scales

over which they take place are consistent with the observations of Guy *et al.* (1966) for flume experiments at larger Froude numbers. Again, with a bed motion at the scale of hours, the approximation of a flow over a steady relief is almost perfect. Consistent with the theory, we did not observe the emergence of wavelengths directly at the scale of the flow depth. Note that in the flume experiments of Carling, Richardson & Ikeda (2005), the large grain size (5 mm) and the moderate water depth (0.375 m) are such that the typical size of the first emerging bedforms (few decimeters) is comparable. We thus reach the conclusion that the formation of dunes should not be associated with a linear instability but to a nonlinear pattern evolution. In the unbounded case (an infinite flow depth), it is probable that this pattern coarsening would have no limit as it is driven by hydrodynamics, which is mostly self-similar. The observation that this coarsening stops at some final wavelength should therefore be associated with a stabilizing mechanism, namely the presence of the free surface.

The places selected for the experiments were of particular interest as different final wavelengths were observed across the river (figure 18*c–e*). The experiments just described above have been performed on the side of the river (say, at a distance less than one third of the river width from the bank). In this 'lateral' region, the sand is well sorted and the dune wavelength is observed to saturate for a rescaled wavenumber kH just below the resonant conditions (figure 19*a*). By contrast, in the central part of the river, much larger bedforms are present (figure 18*d,e*). They display superimposed dunes on their stoss side, and are called mega-dunes hereafter. The river slope and the flow velocity were not significantly different in the dune and mega-dune regions. The major difference was the presence of coarse grains causing bed armouring in the central part of the river. As shown in figure 18(*e*), the transition between the two regions is rather sharp. We have flattened the bed over a zone of 12 m in length and 4 m in width to observe the formation of mega-dunes. The initial stage is the formation of ripples composed of small sand grains that merge, leading to the same dunes as described on the side of the river. However, in the course of this pattern coarsening, the inter-dune zone becomes richer in coarse grains so that the dunes eventually propagate on a bed that is more difficult to erode. They progressively amalgamate into mega-dunes of wavelength ten times larger than the dunes, covered with superimposed ripples and dunes. Even in the asymptotic state, superimposed bedforms are continuously generated. As they propagate faster than the mega-dune, they accumulate at its crest. During the transient of formation of mega-dunes (typically 5 h in our experiments), the pattern is disordered and is not composed by a unique Fourier mode. As far as one can say without having explicitly performed a multi-scale analysis of the topography, structures of growing size were progressively formed, which become ordered as they reach the final mega-dune wavelength (between $10H$ and $20H$).

In summary, a small difference in the experimental conditions (here, most probably, the presence or absence of coarse grains) can significantly affect the pattern coarsening dynamics. The wavelength of mega-dunes can be larger than those of dunes by 1–2 orders of magnitude (figure 19*a*). With this observation, the question is not anymore to find a new destabilizing mechanism to explain the dune formation. Rather, as larger and larger bedforms are produced by nonlinear processes, one needs to identify a stabilizing mechanism limiting this coarsening. As evidenced here, this is exactly the role played by the free surface.

Figure 19 presents several series of measurements of the final bedform wavelength collected in the literature for flume experiments (figure 19*b*) and natural rivers (figure 19*c*). The most important data set is certainly that reported by Guy *et al.* (1966).
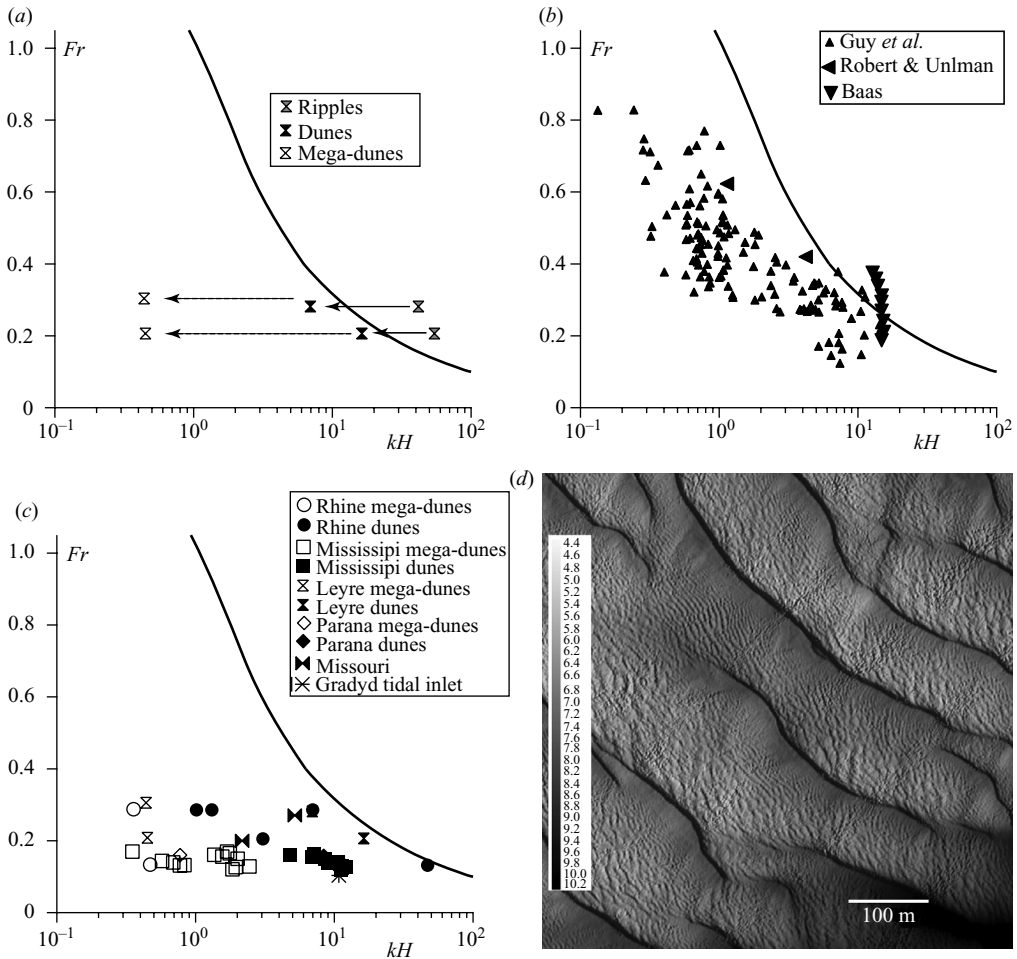
FIGURE 19. Representation in the $\mathscr{F}$ vs. kH diagram of different data sets. The solid line shows the resonant conditions for the free-surface standing waves and separates the supercritical regime (right) from the subcritical one (left). (*a*) Experiments performed in the Leyre river, starting from a flat sand bed. (*b*) Flume experiments: wavelength of the stationary bedforms obtained at long time. (*c*) Bedforms in natural rivers. The mega-dunes are represented by white symbols, whereas dunes are displayed with black symbols. (*d*) Water depth in Rio Paraná ($H \sim 8$ m, $d \sim 300$ μm, $\mathscr{F} = 0.16$) measured by multibeam echo sounding (this photograph is from Parsons *et al.* 2005). Mega-dunes of wavelength $\lambda \sim 125$ m $\sim 15H$ can be observed, with superimposed dunes of wavelength 6 m and probably superimposed ripples too (not visible).

Note that we display these data altogether, i.e. without distinguishing between what they call ripples or dunes (see the introduction). Importantly, Guy *et al.* (1966) have not looked at the transient of formation of bedforms but have focused on the long time regime. For example, they have often started a new experiment with a bed in the state reached at the end of the previous run. Moreover, the control parameters (slope and flow rate) were varied in the course of the experiment to maintain constant secondary quantities such as the flow depth or the Froude number. This methodology is probably responsible for the lack of reproducibility and the huge dispersion of data (one decade horizontally) one can see in figure 19(*b*). By contrast, the series of experiments performed by Baas (1999) are much more controlled and reproducible. In particular, the wavelength is measured as a function of time starting from a flat

sand bed and fitted to obtain its asymptotic value. These flume experiments clearly evidence the difference between the initial wavelength at which ripples form, their evolution by pattern coarsening to form dunes and the nonlinear selection of the final wavelength due to the free surface. Note that we have not taken into account the correction of raw measurements performed by Baas (1999) to take into account the temperature dependence of the viscosity, as it is a nonsense in the hydraulically rough regime. The last points in figure 19(*b*) have been obtained by Robert & Uhlman (2001). As for Guy *et al.* (1966), we have not taken into account the denomination of the bedforms (ripple or dunes) used in this article. The points obtained by Baas (1999) and Robert & Uhlman (2001) are very close to the resonant conditions; the whole data set of Guy *et al.* (1966) is clearly in the subcritical regime – at low $\mathscr{F}$ and/or low wavenumber kH – and globally follows the resonance curve. We have gathered in figure 19(*c*) the points measured in the Leyre river, in the Gràdyd tidal channel (Bartholdy *et al.* 2005), in the Mississipi river (Harbor 1998), in the Missouri river (Annambhotla *et al.* 1972), in the Rhine (Carling *et al.* 2000; Wilbers & Ten Brinke 2003) and in the Rio Paraná (Parsons *et al.* 2005). One can observe that the dunes propagating on the stoss slope of mega-dunes lie in the same region of the diagram as the simple dunes – roughly between $kH = 0.1/\mathscr{F}^2$ and $kH = 1/\mathscr{F}^2$. The mega-dunes lie between $kH = 0.3$ and $kH = 0.1/\mathscr{F}^2$. It should be emphasized that the different points in this graph correspond to very different flow depth H (compare e.g. the mega-dunes in the Leyre river shown in figure 17*d* and those in the Rio Paraná shown in figure 19*d*). It means that the saturation length, which determines the wavelength at which ripples form, is not a relevant length for the formation of dunes and mega-dunes.

5.3. *Denomination of bedforms*

We then see why a distinction between ripples and dunes based on some absolute dimension considerations is misleading from the physical point of view: depending on the value of the water depth, bedforms 'of less than about 2 feet' (Guy *et al.* 1966) or 'less than 0.6 m' (Ashley 1990) can feel or not the free surface. Nor a criterion based on the amplitude $|\delta|\zeta$ of distortion of the free surface can be satisfying to define dunes. Indeed, the free surface is distorted by less than 10 % of the bedform amplitude for $\mathscr{F} < 0.35$ or for $kH > 3$. With a definition based on the amplitude of distortion of the free surface such as that proposed by Guy *et al.* (1966), there would be no dune at all in natural rivers! Approaching $\mathscr{F} = 1$ from below, the distortion of the free surface, in antiphase with the topography, becomes more and more pronounced. Above $\mathscr{F} \simeq 0.6$, this effect becomes sufficient to create a zone of stable wavelengths around the resonance (figure 16) and thus a gap difficult to cross during the pattern coarsening.

These results then suggest a new classification of river bedforms based on the dynamical mechanisms responsible for their formation. The most obvious criterion is the sensitivity to the presence of the free surface. We thus define ripples as the bedforms whose wavelength λ is sufficiently small compared to the flow depth H not to feel the finiteness of the flow depth. In the diagram $\mathscr{F}$ versus kH, they are located in the supercritical region, i.e. their wavenumber is larger than the resonant value. When the scale separation between the flow depth and the saturation length is sufficient, the structures that form by linear instability of a flat sand bed are ripples. Beyond the linear regime the pattern coarsening leads to growing wavelengths that reach the resonance curve. Once in the subcritical region on the left of this curve (figure 19) hydrodynamics becomes affected and in some case dominated by the

presence of the free surface and the bedforms can be called dunes. As evidenced by our field experiments, the pattern coarsening can end with very different bedforms depending on the conditions (e.g. the grain size distribution). The associated nonlinear selection of pattern wavelength is an open problem (Politi & Misbah 2004; Andreotti *et al.* 2006) that will require specific investigations. Our observations suggest to define mega-dunes as bedforms sufficiently large to present superimposed dunes. It is worth noting that dunes can present superimposed ripples when the scale separation between the flow depth H and the saturation length L_{sat} is sufficient. The criterion to separate dunes from mega-dunes is then based on the location of the superimposed bedforms with respect to the resonance curve in the plane $\mathscr{F}$ versus kH. This distinction is important, as in very deep water, the pattern coarsening would lead to ripples large enough to accommodate superimposed ripples on their stoss side. In this case, one should talk about mega-ripples. In summary, the appellation of given subaqueous bedforms should be chosen in function of their location in the diagram $\mathscr{F}$ versus kH, with an additional suffix 'mega-' to point out the presence of superimposed structures.

6. Conclusion

In this article, we have performed the linear stability analysis of a flat sand bed. The destabilizing mechanism is of hydrodynamical nature and is related to the phase advance of the basal shear stress with respect to the topography. Two stabilizing mechanisms are identified: the sediment transport saturation length L_{sat} and the slope effect, which depends on the ratio u_*/u_{th}. As L_{sat} is generically larger than z_0, it dominates and the most growing wavelength λ_{max} is the product of a prefactor related to hydrodynamics by the saturation length. This most unstable mode is associated with ripples, which thus form by a linear instability. In the case of a smooth bottom, the roughness seen from the inner layer is governed by the viscous length ν/u_*, which may dominate the scaling of λ_{max} if ν/u_* is larger than L_{sat} (Sumer & Bakioglu 1984).

Because of the slope effect, the ratio λ_{max}/L_{sat} is a decreasing function of u_*/u_{th}. We have analysed different sets of measurements of initial ripple wavelengths λ_{max} available in the literature and deduced the corresponding saturation length, assuming that the hydrodynamical model is correct. Note that L_{sat} is found roughly independent of u_* and between $5\,d$ and $15\,d$. These values are consistent with a saturation length limited by the grain inertia ($L_{sat} \simeq 2(\rho_s/\rho_f)\,d$) as previously stated by the authors (Claudin & Andreotti 2006; Andreotti & Claudin 2007). This prediction is especially good for large grains ($d \gtrsim 1$ mm), for which viscous effects are completely negligible. However, the data show systematic dependencies that are not captured by the present model: the wavelength at which ripples form is systematically larger for smaller or rougher grains.

We have performed field experiments in the Leyre river, whose results show that the evolution of the ripple wavelength λ and amplitude ζ at short time is consistent with a linear instability. We also observed that these ripples present a pattern coarsening: their wavelength grows and saturate just after crossing the resonance condition of surface waves. In the course of this pattern coarsening, the bedforms are in quasi-equilibrium between erosion and deposition.

The influence of the river free surface on the bed is stabilizing. Gravity waves excited at the free surface by the bedforms are in phase at small λ/H (supercritical regime) and in antiphase at large λ/H (subcritical regime). In between, the free surface is phase advanced with respect to the bottom, so that it tends to induce a phase delay of the shear stress on the ground. Bedforms of wavelength around the

resonance conditions are thus stabilized. Moreover, at very large λ/H, the inner layer invades the whole flow and the free surface again has a strong stabilizing effect. As no destabilizing mechanism is associated with the presence of the free surface, dunes do not form by a linear instability. This result is directly confirmed by our field experiments showing that they form by nonlinear pattern coarsening, as suggested by Raudkivi & Witte (1990) and Raudkivi (2006). Our experiments also show that the nonlinear selection of the final wavelength is very sensitive to small changes in the experimental conditions, and in particular to the presence of coarse grains.

Finally, our results suggest to classify subaqueous bedforms according to the dynamical mechanisms that control their formation. We thus propose the following bedform definitions and characteristics.

(i) Ripples are bedforms whose wavelength λ is sufficiently small compared to the flow depth H not to feel the presence of the free surface. In the diagram $\mathscr{F}$ versus kH, they are located on the right of the resonance curve (supercritical regime). They form by linear instability and their initial wavelength essentially scales on the saturation length L_{sat}. They exhibit pattern coarsening and remain ripples until they cross the condition of resonance of the surface waves.

(ii) Dunes are bedforms whose wavelength λ is sufficiently large compared to the flow depth H to be stabilized by the presence of the free surface. The ripple pattern coarsening generically leads to the formation of dunes. In the diagram $\mathscr{F}$ versus kH, they are located along the resonance curve on the subcritical side. If the flow depth H is much larger than the wavelength at which ripples form, dunes may present superimposed ripples.

(iii) Like dunes, mega-dunes are under the influence of the free surface and on the left side of the resonance curve but they present superimposed dunes. They typically result from the coarsening of a dune pattern pushed to very large wavelength by heterogeneities (in particular a polydispersed sediment).

Further studies are needed to investigate this nonlinear wavelength selection in details. For the purpose of describing the interactions between bedforms, future models will have to incorporate hydrodynamical nonlinearities and in particular flow separation.

Supplementary material is available at journals.cambridge.org/FLM.

REFERENCES

ALLEN, J. R. L. 1985 *Principles of Physical Sedimentology*. Blackburn Press.

ANDERSON, R. 1987 A theoretical model for aeolian impact ripples. *Sedimentology* **34**, 943–956.

ANDERSON, R. 1990 Eolian ripples as examples of self-organization in geomorphological systems. *Earth-Science Rev.* **29**, 77–96.

ANDREOTTI B. 2004 A two species model of aeolian sand transport. *J. Fluid Mech.* **510**, 47–50.

ANDREOTTI, B. & CLAUDIN, C. 2007 Comment on 'Minimal size of a barchan dune'. *Phys. Rev.* E **76**, 063301.

ANDREOTTI, B. & CLAUDIN, C. 2009 On the different regimes of subaqueous transport. *Eur. Phys. J. B* (submitted) arXiv:0910.4119.

ANDREOTTI, B., CLAUDIN, P. & DOUADY, S. 2002 Selection of dune shapes and velocities. Part 2. A two-dimensional modelling. *Eur. Phys. J. B* **28**, 341–352.

ANDREOTTI, B., CLAUDIN, P. & POULIQUEN, O. 2006 Aeolian sand ripples: experimental evidence of coarsening and saturation. *Phys. Rev. Lett.* **96**, 028001.

ANDREOTTI, B., CLAUDIN, C. & POULIQUEN, O. 2009 Measurements of the aeolian sand transport saturation length. *Geomorphology* (submitted) arXiv:0806.3931.

ANNAMBHOTLA, V. S. S., SAYRE, W. W. & LIVESEY, R. H. 1972 Statistical properties of Missouri River bed forms. *J. Waterways Harbors Coastal Engng Div.* **98**, 489–510.

ASHLEY, G. M. 1990 Classification of large scale subaqueous bedforms: a new look at an old problem. *J. Sedim. Res.* **60**, 161–172.

AYOTTE, K. W., XU, D. & TAYLOR, P. A. 1994 The impact of turbulence closure schemes on predictions of the mixed spectral finite-difference model for flow over topography. *Boundary-Layer Met.* **68**, 1–33.

BAAS, J. H. 1994 A flume study on the development and equilibrium morphology of current ripples in very fine sand. *Sedimentology* **41**, 185–209.

BAAS, J. H. 1999 An empirical model for the development and the equilibrium morphology of current ripples in fine sand. *Sedimentology* **46**, 123–138.

BAGNOLD, R. A. 1941 *The Physics of Blown Sand and Desert Dunes*. Methuen.

BAGNOLD, R. A. 1956 The flow of cohesionless grains in fluids. *Phil. Trans. R. Soc. London* A **249**, 235–297.

BARTHOLDY, J., FLEMMING, B. W., BARTHOLOMÄ, A. & ERNSTSEN, V. B. 2005 Flow and grain size control of depth-independent simple subaqueous dunes. *J. Geophys. Res.* **110**, F04S16.

BELCHER, S. E. & HUNT, J. C. R. 1998 Turbulent flow over hills and waves. *Ann. Rev. Fluid Mech.* **30**, 507–538.

BELJAARS, A. C. M. & TAYLOR, P. A. 1989 On the inner-layer scale height of boundary-layer flow over low hills. *Boundary-Layer Met.* **49**, 433–438.

BENJAMIN, T. B. 1959 Shearing flow over a wavy boundary. *J. Fluid Mech.* **6**, 161–205.

BEST, J. 2005 The fluid dynamics of river dunes: a review and some future research directions. *J. Geophys. Res.* **110**, F04S02.

BORDNER, G. L. 1978 Nonlinear analysis of laminar boundary layer flow over a periodic wavy surface. *Phys. Fluids* **21**, 1471–1464.

BRITTER, R. E., HUNT, J. C. R. & RICHARDS, K. J. 1981 Air flow over a two-dimensional hill: studies of velocity speed-up, roughness effects and turbulence. *Q. J. R. Meteorol. Soc.* **107**, 91–110.

CAPONI, E. A., FORNBERG, B., KHIGHT, D. D., MCLEAN, J. W., SAFFMAN, P. G. & YUEN, H. C. 1982 Calculations of laminar viscous flow over a moving wavy surface. *J. Fluid Mech.* **124**, 247–262.

CARLING, P. A., GÖLZ, E., ORR, H. G. & RADECKI-PAWLIK, A. 2000 The morphodynamics of fluvial sand dunes in the River Rhine, near Mainz, Germany. I. Sedimentology and morphology. *Sedimentology* **47**, 227–252.

CARLING, P. A., RICHARDSON, K. & IKEDA, H. 2005 A flume experiment on the development of subaqueous fine-gravel dunes from a lower-stage plane bed. *J. Geophys. Res.* **110**, F04S05.

CHARRU, F. 2006 Selection of the ripple length on a granular bed. *Phys. Fluids* **18**, 121508.

CHARRU, F. & HINCH, E. J. 2000 'Phase diagram' of interfacial instabilities in a two-layer Couette flow and mechanism for the long-wave instability. *J. Fluid Mech.* **414**, 195–223.

CHARRU, F., LARRIEU, E., DUPONT, J.-B. & ZENITH, R. 2008 Motion of a particle near a rough wall in a viscous shear flow. *J. Fluid Mech.* **570**, 431–453.

CHARRU, F., MOUILLERON-ARNOULD, H. & EIFF, O. 2004 Erosion and deposition of particles on a bed sheared by a viscous flow. *J. Fluid Mech.* **519**, 55–80.

CLAUDIN, P. & ANDREOTTI, B. 2006 A scaling law for aeolian dunes on Mars, Venus, Earth, and for sub-aqueous ripples. *Earth Pla. Sci. Lett.* **252**, 30–44.

CLAUSSEN, M. 1988 On the inner-layer scale height of boundary-layer flow over low hills. *Boundary-Layer Met.* **44**, 411–413.

COLEMAN, S. E. & ELING, B. 2000 Sand wavelets in laminar open-channel flows. *J. Hydraul. Res.* **38**, 331–338.

COLEMAN, S. E., FEDELE, J. J. & GARCIA, M. H. 2003 Closed-conduit bed-form initiation and development. *J. Hydraul. Engng* **129**, 956–965.

COLEMAN, S. E. & FENTON, J. D. 2000 Potential-flow instability theory and alluvial stream bed forms. *J. Fluid Mech.* **418**, 101–117.

COLEMAN, S. E. & MELVILLE, B. W. 1994 Bed-form development. *J. Hydraul. Engng* **120**, 544–560.

COLEMAN, S. E. & MELVILLE, B. W. 1996 Initiation of bed forms on a flat sand bed. *J. Hydraul. Engng* **122**, 301–310.

COLOMBINI, M. 2004 Revisiting the linear theory of sand dune formation. *J. Fluid Mech.* **502**, 1–16.

COLOMBINI, M. & STOCCHINO, A. 2005 Coupling or decoupling bed and flow dynamics: fast and slow sediment waves at high Froude numbers. *Phys. Fluids* **17**, 036602.

EINSTEIN, H. A. 1950 The bed load function for sedimentation in open channel flows. *Tech. Rep.* **1026**, 1–69.

ELBELRHITI, H., CLAUDIN, C. & ANDREOTTI, B. 2005 Field evidence for surface wave induced instability of sand dunes. *Nature* **437**, 720–723.

ENGELUND, F. 1970 Instability of erodible beds. *J. Fluid Mech.* **42**, 225–244.

ENGELUND, F. & FREDSØE, J. 1982 Sediment ripples and dunes. *Ann. Rev. Fluid Mech.* **14**, 13–37.

FERNANDEZ LUQUE, R. & VAN BEEK, R. 1976 Erosion and transport of bed-load sediment. *J. Hydraul. Res.* **14**, 127–144.

FINNIGAN, J. J., RAUPACH, M. R., BRADLEY, E. F. & ALDIS, G. K. 1990 A wind tunnel study of turbulent flow over a two-dimensional ridge. *Boundary-Layer Met.* **50**, 277–317.

FREDSØE, J. 1974 On the development of dunes in erodible channels. *J. Fluid Mech.* **64**, 1–16.

GONG, W. & IBBETSON, A. 1989 A wind tunnel study of turbulent flow over model hills. *Boundary-Layer Met.* **49**, 113–148.

GRADOWCZYK, M. H. 1970 Wave propagation and boundary instability in erodible-bed channels. *J. Fluid Mech.* **33**, 93–112.

GUY, H., SIMONS, D. & RICHARDSON, E. 1966 Summary of alluvial channel data from flume experiments, 1956–61. *U.S. Geol. Survey Prof. Paper* **462-I**, 1–96.

GYR, A. & SCHMID, A. 1989 The different ripple formation mechanism. *J. Hydraul. Res.* **27**, 61–74.

HARBOR, D. J. 1998 Dynamics of bedforms in the lower Mississippi River. *J. Sedim. Res.* **68**, 750–762.

HAYASHI, T. 1970 Formation of dunes and antidunes in open channels. *J. Hydraul. Div.* **96**, 357–366.

HERSEN, P., DOUADY, S. & ANDREOTTI, B. 2002 Relevant length scale of barchan dunes. *Phys. Rev. Lett.* **89**, 264–301.

HILL, H. M., SRINIVASAN, V. S. & UNNY, T. E. 1969 Instability of flat bed in alluvial channels. *J. Hydraul. Div.* **95**, 1545–1558.

HUNT, J. C. R., LEIBOVICH, S. & RICHARDS, K. J. 1988 Turbulent shear flows over low hills. *Q. J. R. Meteorol. Soc.* **114**, 1435–1470.

JACKSON, P. S. & HUNT, J. C. R. 1975 Turbulent wind flow over a low hill. *Q. J. R. Meteorol. Soc.* **101**, 929–955.

KAMPHUIS, J. W. 1974 Determination of sand roughness for fixed beds. *J. Hydraul. Res.* **12**, 193–207.

KENNEDY, J. F. 1963 The mechanics of dunes and antidunes in erodible bed channels. *J. Fluid Mech.* **16**, 521–544.

KENNEDY, J. F. 1969 The formation of sediment ripples, dunes and antidunes. *Annu. Rev. Fluid Mech.* **1**, 147–168.

KOBAYASHI, N. & MADSEN, O. S. 1985 Turbulent flows over a wavy bed. *J. Geophys. Res.* **90**, 7323–7331.

KROY, K., SAUERMANN, G. & HERRMANN, H. J. 2002 Minimal model for aeolian sand dunes. *Phys. Rev. E* **66**, 031302.

LAGRÉE, P.-Y. 2003 A triple deck model of ripple formation and evolution. *Phys. Fluids* **15**, 2355–2368.

LANGLOIS, V. & VALANCE, A. 2007 Formation and evolution of current ripples on a flat sand bed under turbulent water flow. *Eur. Phys. J. E* **22**, 201–208.

LOISELEUX, T., GONDRET, P., RABAUD, M. & DOPPLER, D. 2005 Onset of erosion and avalanche for an inclined granular bed sheared by a continuous laminar flow. *Phys. Fluids* **17**, 103304.

MANTZ, P. A. 1978 Bedforms produced by fine, cohesionless, granular and flakey sediments under subcritical water flows. *Sedimentology* **25**, 83–103.

McLean, S. R. 1990 The stability of ripples and dunes. *Earth-Science Rev.* **29**, 131–144.

Meyer-Peter, E. & Müller, R. 1948 Formulas for bed load transport. *Report on the 2nd Meeting International Association Hydraulic Structure Research, Stockholm*, pp. 39–64.

Parker, G. 1975 Sediment inertia as cause of river antidunes. *J. Hydraul. Div.* **101**, 211–221.

Parsons, D. R., Best, J. L., Orfeo, O., Hardy, R. J., Kostaschuk, R. & Lane, S. N. 2005 Morphology and flow fields of three-dimensional dunes, Rio Paraná, Argentina: results from simultaneous multibeam echo sounding and acoustic Doppler current profiling. *J. Geophys. Res.* **110**, F04S03.

Perry, A. E., Schofield, W. H. & Joubert, P. N. 1969 Rough wall turbulent boundary layers. *J. Fluid Mech.* **37**, 383–413.

Politi, P. & Misbah, C. 2004 When does coarsening occur in the dynamics of one-dimensional fronts. *Phys. Rev. Lett.* **92**, 090601.

Prandtl, L. 1925 Bericht über Untersuchungen zur ausgebildeten Turbulenz. *Z. Ang. Math. Mech.* **3**, 136–139. (After, Bradshaw, P. 1974 Possible origin of Prandt's mixing-length theory. *Nature* **249**, 135–136.)

Raudkivi, A. J. 2006 Transition from ripples to dunes. *J. Hydraul. Engng* **132**, 1316–1320.

Raudkivi, A. J. & Witte, H. H. 1990 Development of bed features. *J. Hydraul. Engng* **116**, 1063–1079.

Rauen, W. B., Lin, B. & Falconer, R. A. 2008 Transition from wavelets to ripples in a laboratory flume with a diverging channel. *Intl J. Sedim. Res.* **23**, 1–12.

Reynolds, A. J. 1965 Waves on the erodible bed of an open channel. *J. Fluid Mech.* **22**, 113–133.

Reynolds, O. 1874 On the extent and action of the heating surface of steam boilers. *Proc. Lit. Phil. Soc. Manchester* **14**, 7–12.

Richards, K. J. 1980 The formation of ripples and dunes on an erodible bed. *J. Fluid Mech.* **99**, 597–618.

Richards, K. J. & Taylor, P. A. 1981 A numerical model of flow over sand waves in water of finite depth. *Geophys. J. R. Astron. Soc.* **65**, 103–128.

Robert, A. & Uhlman, W. 2001 An experimental study of the ripple-dune transition. *Earth Surf. Process. Landforms* **26**, 615–629.

Sauermann, G., Kroy, K. & Herrmann, H. J. 2001 Continuum saltation model for sand dunes. *Phys. Rev.* E **64**, 031305.

Schlichting, H. & Gersten, K. 2000 *Boundary Layer Theory*, 8th edn. Springer.

Smith, J. D. 1970 Stability of a sand bed subjected to a shear flow at low Froude number. *J. Geophys. Rev.* **75**, 5928–5940.

Sumer, B. M. & Bakioglu, M. 1984 On the formation of ripples on an erodible bed. *J. Fluid Mech.* **144**, 177–190.

Sykes, R. I. 1980 An asymptotic theory of incompressible turbulent boundary-layer flow over a small bump. *J. Fluid Mech.* **101**, 647–670.

Taylor, P. A. 1977*a* Some numerical studies of surface boundary-layer flow above gentle topography. *Boundary-Layer Met.* **11**, 439–465.

Taylor, P. A. 1977*b* Numerical studies of neutrally stratified planetary boundary-layer flow above gentle topography. *Boundary-Layer Met.* **12**, 37–60.

Taylor, P. A., Mason, P. J. & Bradley, E. F. 1987 Boundary-layer flow over low hills. *Boundary-Layer Met.* **39**, 107–132.

Tritton, D. J. 1988 *Physical Fluid Dynamics*. Oxford University Press.

Valance, A. 2005 Formation of ripples over a sand bed submitted to a turbulent shear flow. *Eur. Phys. J.* B **45**, 433–442.

Valance, A. & Langlois, V. 2005 Ripple formation over a sand bed submitted to a laminar shear flow. *Eur. Phys. J.* B **43**, 283–294.

Venditti, J. G., Church, M. A. & Bennett, S. J. 2005*a* Morphodynamics of small-scale superimposed sand waves over migrating dune bed forms. *Water Resour. Res.* **41**, W10423.

Venditti, J. G., Church, M. A. & Bennett, S. J. 2005*b* Bed form initiation from a flat sand bed. *J. Geophys. Res.* **110**, F01009.

Weng, W. S., Hunt, J. C. R., Carruthers, D. J., Warren, A., Wiggs, G. F. S., Linvingstone, I. & Castro, I. 1991 Air flow and sand transport over sand dunes. *Acta Mechanica* **2**, 1–22.

WIGGS, G. F. S. 2001 Desert dune processes and dynamics. *Prog. Phys. Geog.* **25**, 53–79.

WILBERS, A. W. E. & TEN BRINKE, W. B. M. 2003 The response of subaqueous dunes to floods in sand and gravel bed reaches of the Dutch Rhine. *Sedimentology* **50**, 1013–1034.

YALIN, M. S. 1963 An expression for bed-load transportation. *J. Hydraul. Div.* **132**, 1159–1168.

YALIN, M. S. 1977 On the determination of ripple length. *J. Hydraul. Div.* **103**, 439–442.

YALIN, M. S. 1985 On the determination of ripple geometry. *J. Hydraul. Engng* **111**, 1148–1155.

YALIN, M. S. & KARAHAN E. J. 1979 Inception of sediment transport. *J. Hydraul. Div.* **105**, 1433–1443.